Wintertime precipitation over the Australian Snowy Mountains: Observations from an Intensive Field Campaign 2018

Luis Ackermann,[a,b] Yi Huang,[c,b] Steven Siems[a,b], Michael Manton,[a] Francisco Lang,[a] Thomas Chubb,[d] Andrew Peace[d], Johanna Speirs[d], Kenyon Suzanne[d], Alain Protat[e], Simon P. Alexander[f,g].

[a] *School of Earth, Atmosphere and Environment, Monash University, Melbourne, Victoria, Australia*

[b] *Australian Research Council (ARC) Centre of Excellence for Climate System Science, Monash University, Melbourne, Victoria, Australia*

[c] *School of Earth Sciences, The University of Melbourne, Melbourne, Victoria, Australia*

[d] *Snowy Hydro Limited, Sydney, New South Wales, Australia*

[e] *Australian Bureau of Meteorology, Melbourne, Victoria, Australia*

[f] *Australian Antarctic Division, Kingston, Tasmania, Australia*

[g] *Australian Antarctic Program Partnership, Institute of Marine and Antarctic Studies, Hobart, TAS, Australia*

Corresponding author: Luis Ackermann, luis.ackermann@monash.edu

Early Online Release: This preliminary version has been accepted for publication in *Journal of Hydrometeorology,* may be fully cited, and has been assigned DOI 10.1175/JHM-D-20-0283.1. The final typeset copyedited article will replace the EOR at the above DOI when it is published.

ABSTRACT

Understanding the key dynamical and microphysical mechanisms driving precipitation in the Snowy Mountains region of southeast Australia, including the role of orography, can help improve precipitation forecasts, which is of great value for efficient water management. An intensive observation campaign was carried out during the 2018 austral winter, providing a comprehensive range of ground-based observations across the Snowy Mountains. We used data from three vertically pointing rain radars, cloud radar, a PARSIVEL disdrometer, and a network of 76 pluviometers. The observations reveal that all of the precipitation events were associated with cold front passages. About half accumulated during the frontal passage associated with deep, fully glaciated cloud tops; while the rest occurred in the post-frontal environment and was associated with clouds with supercooled liquid water (SLW) tops. About three quarters of the accumulated precipitation were observed under blocked conditions, likely associated with blocked stratiform orographic enhancement. Specifically, more than a third of the precipitation resulted from moist cloudless air being lifted over stagnant air, upwind from the barrier, creating SLW-top clouds. These SLW-clouds then produced stratiform precipitation mostly over the upwind slopes and mountain tops, with hydrometeors reaching the mountain tops mostly as rimed snow. Two precipitation events were studied in detail, which showed that during unblocked conditions, orographic convection invigoration and unblocked stratiform enhancement were the two main mechanisms driving the precipitation; with the latter being more prevalent after the frontal passage. During these events, ice particle growth was likely dominated by vapor deposition and aggregation during the frontal periods, while riming dominated during the post-frontal periods.

Accepted for publication in *Journal of Hydrometeorology*. DOI 10.1175/JHM-D-20-0283.1.

SIGNIFICANCE STATEMENT

We need to be able to improve precipitation forecast over the Snowy Mountains to help improve water management efficiency in the region. Precipitation in this region accounts for a third of the inflow to the Murray-Darling basin, which produces about 22 billion AUD per year in agricultural and industrial activities. With this aim, we carried novel observations during the 2018 austral winter with advanced instruments at 3 different locations in the mountains, supported by a network of 72 pluviometers in this region. This campaign provided insights on how the orography enhances precipitation, which microphysical processes are dominant, and created a benchmark dataset to evaluate in detail future modeling studies.

1. Introduction

Precipitation over the Snowy Mountains in southeast Australia is of great economic and scientific interest. The Snowy Mountains form part of the Australian Great Dividing Range, and include the highest terrain in Australia with a peak elevation of 2,228 m above sea level (ASL). Precipitation that falls in the region forms the headwaters of the Snowy River, that flows east to the Tasman Sea, as well as the Murray and Murrumbidgee Rivers that flow west into the Murray-Darling Basin. Precipitation over the Snowy Mountains accounts for roughly a third of the inflow into the Murray-Darling Basin, a region that produces about $22 billion (AUD) per year in agricultural activities and more than one-third of Australia's food supply (MDBA 2017). Further, Snowy Hydro Limited (hereafter "Snowy Hydro"), the hydroelectric company managing water resources in the area, actively redistributes water towards the

Murray-Darling Basin that would otherwise flow into the Tasman Sea. Snowy Hydro also employs these resources to generate hydroelectric power.

Scientifically, clouds over the Snowy Mountains and their precipitation are of increasing interest given their unique nature, which includes the frequent occurrence of supercooled liquid water (SLW) during the winter wet season (May-September; Morrison et al. 2013; Osburn et al. 2016). Employing MODIS (Moderate Resolution Imaging Spectroradiometer) satellite products, Morrison et al. (2013) found that SLW was observed at cloud-top ~40-50% of the time across the Snowy Mountains, Victorian Alps and central highlands of Tasmania, which is a factor of two greater than the peak frequency of SLW over western continental United States where cloud seeding programs have been undertaken. In the Colorado Rockies, SLW was observed about a quarter of the time during winter and these clouds were associated with snow riming (Hindman, 1986). Furthermore, a modeling study by Saleeby et al (2013) focusing on the development of precipitation within SLW orographic clouds predicted areas of enhanced vapor deposition near the top of the windward slopes, while riming was maximized over the ridge and close to the surface. These SLW clouds have been shown to commonly occur in post-frontal conditions when a pristine Southern Ocean air mass is forced over the mountains (Chubb et al. 2011, 2013). Given the regularity of such conditions, the Snowy Mountains offer a unique environment to study the microphysics of mixed-phase clouds and the development of precipitation under such conditions.

Clouds overpassing mountainous terrain can be affected by the orography in a variety of complex ways. Houze (2012) identified 12 distinct mechanisms for orographic precipitation enhancement; which mechanism is at play depends on multiple factors such as the type of synoptic system, the geometry of the mountain, the upwind stability, and the aerosol content. Manton et al. (2017) analyzed field observations over the Snowy Mountains to demonstrate

the sensitivity of the precipitation to orographic blocking. Depending on the upwind stability, the incoming air mass can become stagnant over the windward slope (blocked) or ascend over the barrier with no deceleration (unblocked). The relationship between precipitation and whether or not the flow is blocked is complex and can favor certain orographic mechanisms over others.

Given the importance of this precipitation, developing a precipitation climatology over the Snowy Mountains has been the subject of numerous efforts (e.g. Nicholls 2005; Murphy and Timbal 2008; Timbal 2009; Chubb et al. 2011, 2016b, 2015; Theobald et al. 2015). Many recent efforts (e.g. Sarmadi et al. 2019b) have relied upon the Australian Water Availability Project (AWAP; Jones et al. 2009) for the precipitation analysis. However, using an independent network of high-altitude rain gauges, Chubb et al. (2016b) found precipitation to be underestimated by as much as 18% compared to AWAP-derived precipitation across the Murray catchment. This bias was most pronounced along the windward slopes, primarily due to the low density of gauges in the area and a lack of accounting for any upwind/downwind orographic processes in the analysis algorithm.

Intensive field campaigns can improve the understanding of the processes behind orographic precipitation, helping to reduce biases in both operational forecasts and reanalysis algorithms. One such campaign was carried out in Tug Hill, east of Lake Ontario, the United States, where the effect of orographic uplift on air masses was studied using profiling micro rain radars. It was found that the terrain height was associated with a transition from a convective to stratiform morphology (Minder et al. 2015). Another field campaign in the northwestern United States aimed to improve quantitative precipitation forecasting and bulk microphysical parameterization schemes (Stoelinga et al. 2003). French et al. (2018) describes an intensive field observation campaign that showed the initiation, growth and

precipitation of ice crystals during winter over the Payette Mountains of southwestern Idaho; specifically documenting how glaciogenic seeding affected these processes. We note that Snowy Hydro maintains operational cloud seeding across the Snowy Mountains (Manton et al. 2011; Manton and Warren 2011; Manton et al. 2017), given the frequent presence of SLW.

Motivated by the success of these orographic field campaigns in the United States, the lack of such observations in our area of interest which has a much larger fraction of SLW cloud than in the US, and the need to improve our understanding of the processes associated with orographic precipitation in this region, we conducted an intensive ground-based measurement campaign during the austral winter in 2018. A primary aim of this campaign has been to document and understand the development and evolution of precipitation in mixed-phase conditions arising from orographic forcing, which is presented herein. Such observations can then be employed to evaluate both numerical simulations and precipitation analyses, which is the subject of future work.

2. Methods

2.1 Observation campaign

The campaign started on the 25th of July 2018 and ended on the 7th of September 2018 (44 days). It consisted of three primary surface sites (Figure 1): an upwind site west of the Snowy Mountains at Murray-1 (a power station at elevation 337 m ASL), a near-peak site which is downwind of Murray-1 during the prevailing westerly winds (Blue Cow; 1,901 m ASL) and a site to the north of Blue Cow (Cabramurra; 1488 m ASL) where a steep terrain exposed to prevailing winds is present. While the locations of the primary sites were constrained by logistical considerations, the alignment allowed for a study of the evolution of

the meteorology both transverse and aligned with the ridge axis of the Snowy Mountains. A suite of advanced instruments was installed at Cabramurra, while a limited set of instruments were placed at Murray-1 and Blue-Cow. Surface observations of precipitation, maintained by Snowy Hydro, were spread across 76 sites spanning the domain (Figure 1). 50 of these 76 sites had surface weather observations. A summary of the instruments, locations, and measurements can be found in Table 1 while detailed description of the instruments can be found in the supplemental material section 1.

2.2 Analysis

SYNOPTIC CLASSIFICATION

Wintertime precipitation in the Snowy Mountains is predominantly governed by mid-latitude systems associated with the circumpolar storm track over the Southern Ocean (Chubb et al. 2011; Ryan and Wilson 1984; Pook et al. 2006; Theobald et al. 2015). These frontal systems commonly exhibit a split upwind of Tasmania resulting in fewer cyclones between 45˚ and 55˚S but higher frequencies north and south of this latitude band (Simmonds and Keay 2000). This phenomenon naturally segregates the passing systems into cut-off lows (north of 45˚S) and embedded lows (south of 45˚S). Cold fronts are a common feature of these cyclonic systems and are the primary driver of wintertime precipitation. Following Chubb et al. (2011), precipitation events in this region can be segregated into 5 categories: embedded lows with fronts, embedded lows without fronts, cut-off lows with fronts, cut-off lows without fronts, and other. Although all cold fronts are associated with cyclonic systems, not all cyclonic systems exhibit well-defined cold fronts.

PRECIPITATION EVENT DEFINITION

Accepted for publication in *Journal of Hydrometeorology*. DOI 10.1175/JHM-D-20-0283.1.

In this study, a precipitation event is defined when the accumulated precipitation (liquid equivalent) reaches or exceeds 4 mm at Cabramurra. An event begins with the first measurement of precipitation at this site and ends at any break in precipitation of six hours or longer. Different values for this gap in precipitation window between events were investigated; the period could be changed from 4 to 8 hours for the campaign without changing the number of observed events or the accumulated precipitation per event. By these definitions, ten events were recorded during the campaign. If the accumulation threshold was set to zero, three additional minor events were identified which combined account for 6.5 mm (<2% of total).

FRONTAL VS. POST-FRONTAL CLASSIFICATION

The ten precipitation events were segregated into frontal and post-frontal periods using Mean Sea Level Pressure (MSLP) charts and surface temperature and wind observations, in conjunction with Himawari-8 satellite images of the deep frontal cloud bands (Miller et al. 2016). Precipitation recorded before and during the passage of the deep frontal cloud bands was classified as frontal, while precipitation recorded after the cloud bands passed was classified as post-frontal.

LOW-LEVEL FLOW REGIMES

The low-level flow regimes, whether low-level winds will go over the mountain or be stagnated/diverted laterally around the mountain barrier, can be estimated from the square of the non-dimensional mountain height ($\hat{H}^2$) or, synonymously, the reciprocal of the Froude number. With $\hat{H}^2 < 1$ indicating that low-level winds will go over the mountain, and $\hat{H}^2 > 1$ indicating that low-level winds will be stagnated or diverted laterally around the mountain barrier (Smith 1980).

$\hat{H}^2$ is defined as $(N^2 h^2) / U^2_L$. Where N is the Brunt-Väisälä frequency (s^{-1}), h is the effective barrier height (a constant equal to 1600 m for this mountain range), and U is the cross-barrier wind speed (m s^{-1}). To calculate U, the ridge axis was defined as being at 30 degrees from North (Figure 1, yellow dashed line), and the normal component to this angle was used in the equation. $\hat{H}^2$ was calculated using the same methodology as in Sarmadi et al. (2017) for a location close to Albury, NSW in relatively flat and low-lying terrain (~230 m ASL), approximately 100 km upwind (west) of Cabramurra (see supporting information section 3 for details). Good agreement was found when comparing $\hat{H}^2$ calculated from the physical soundings near Murray-1 and virtual soundings created from the ECMWF Reanalysis v5 (ERA5; Hersbach et al. 2020), therefore hourly time series of $\hat{H}^2$ were created from ERA5 for the duration of the campaign. Times where $\hat{H}^2 > 1$ will be hereafter referred to as blocked, meaning low-level winds should, in theory, stagnate or go around the mountain, while upper-level winds will still cross the mountain. Times when $\hat{H}^2 < 1$ will be hereafter referred to as unblocked. We note that $\hat{H}^2 = 1$is an ideal threshold, rather than an exact one. Only periods of positive (from northwest to southeast) cross mountain winds will be considered valid for this classification; this criterion excludes 1.5% of the precipitation observed in the campaign.

DATA SEGREGATION AND SUBSETS

The data were further segregated by blocking into 4 subsets: Unblocked & Frontal (UF), Blocked & Frontal (BF), Unblocked & Post-frontal (UP), and Blocked & Post-frontal (BP). The segregation was applied strictly to precipitation events only, and do not include times when no precipitation was observed. Further we clarify that we define blocking strictly as orographic blocking as opposed to synoptic blocking.

Accepted for publication in *Journal of Hydrometeorology*. DOI 10.1175/JHM-D-20-0283.1.

The pluviometer sites were subdivided to quantify the spatial variability of precipitation, specifically with respect to the distance to the ridge axis. The categories defined were Upwind, High-altitude, and Downwind (see Figure 1).

3. Results / Discussions

3.1 2018 seasonal precipitation

To assess precipitation characteristics in 2018 compared to climatology, seven of the 76 pluviometer sites were selected for their altitude, data availability (more than 20 years at 30-minute resolution), and quality of the instrumentation (see Table 2 for site details). The accuracy and reliability of these sites have been evaluated and found appropriate for climatological studies (Chubb et al. 2011, 2016b; Sarmadi et al. 2019). Wintertime (May-Oct) precipitation in 2018 was well below average compared to the 1995-2015 climatology, with the seven sites receiving only about half of the long-term mean winter precipitation. 2006 was the only year in the climatological record drier than 2018. Dry conditions in 2018 were widespread across much of eastern Australia, linked to cool sea surface temperatures around tropical Australia associated with the Indian Ocean Dipole and El Nino Southern Oscillation climate patterns (Ades et al. 2019; Australian Bureau Of Meteorology 2018). Although the 2018 winter season was abnormally dry in the Snowy Mountains, frequent precipitation events were observed during the intensive campaign (especially in August). For the six-week period, the accumulated precipitation was very similar to the climatological mean accumulated precipitation. In spite of these 'average conditions' during the actual campaign, we acknowledge the potential that these observations may not be fully representative given the anomalous seasonal precipitation.

Accepted for publication in *Journal of Hydrometeorology*. DOI 10.1175/JHM-D-20-0283.1.

3.2 Orographic effects on precipitation

3.2.1 PLUVIOMETER NETWORK

Seeking to better understand the distribution and variability of the precipitation, data from the 76 pluviometers were analyzed with respect to frontal period, upwind stability, and distance from the ridge axis. A strong orographic signature was observed (Figure 2c), with greater accumulated precipitation on the upwind sites (~38%) and the high-altitude sites (~54%), and only ~9% of the precipitation occurring at the downwind sites.

The proportion of total precipitation between the upwind, downwind and high-altitude sites is similar during both the frontal and post-frontal periods (Table 3), although slightly more precipitation was received at the upwind sites during frontal conditions and in the high-altitude sites during post-frontal conditions. As a whole, post-frontal periods accounted for 53% of the total precipitation, and favored the southern part of the region (Figure 2b and 2d) where the elevation is greatest. For the high-altitude sites, about a third more precipitation is observed (Figure 1c) in post-frontal periods than during frontal periods.

The upwind stability is found to have a stronger impact on precipitation than the time relative to the frontal passage (Figure 3), with 74% of the precipitation occurring during blocked conditions (BF plus BP). Furthermore, blocked conditions lead to greater upwind/high-altitude precipitation ratios both during and after the front passage. Blocked conditions also produced enhanced precipitation observations in the windward slopes, consistent with Micro Rain Radar (MRR) observations at Cabramurra (as discussed in Section 3.2.2 below). It is important to note that total accumulations do not necessarily indicate higher precipitation intensities. Indeed, while the BP subset recorded the most precipitation (42%) it also had the lowest mean precipitation intensity (0.3 mm hr^{-1}).

Accepted for publication in *Journal of Hydrometeorology*. DOI 10.1175/JHM-D-20-0283.1.

3.2.2 RADAR REFLECTIVITY, ZE

Radar reflectivity (Ze) profiles can be used to infer information about particle growth (related to the slope of the Ze) and overall precipitation intensity (relative to the absolute value of Ze), with higher Ze values usually indicating larger hydrometeors. These profiles can be made with respect to temperature instead of height (if the temperature profile is known) which can provide clues regarding the phase of the hydrometeors and the likely microphysical processes occurring. The temperature profiles were determined from reanalysis (ERA5) since the radiosondes were too sparse. Median Ze and Radial Velocity (VR) profiles for each MRR site (Murray-1, Cabramurra, and Blue Cow) were calculated at 1 ˚C bins (Figure 4) with ± one standard deviation for the four subdivisions UF, BF, UP, and BP to elucidate the influences of frontal passages and stability that underpin the hydrometeors growth. Negative VR values show hydrometeors moving down towards the instrument. Only data at temperatures below freezing are shown, in order to avoid potentially large errors in the calculation of the median profiles arising from small errors in the ERA5 atmospheric temperature profile, associated with the bright Ze band at the melting layer. Note that Figure 4 is a composite of multiple events. To avoid single events driving the medians towards the very low or high temperatures ranges, a minimum data threshold (90 for the MRR-2 and 315 for the MRR-Pro) was set; any temperature bins with less than this data threshold for each site was excluded from the figure.

During UF periods (Figure 4a & 4b), all sites show similar Ze profiles, with overall negative Ze slopes (i.e. decreasing Ze against increasing altitude/decreasing temperature), which indicates particle growth (or a large increase in particle number) as they precipitate. Relatively warm/shallow precipitation is evident at Cabramurra compared to UP and possibly a secondary Ze maximum is located near -12 ˚C. In addition, Figure 4b reveal infrequent

Accepted for publication in *Journal of Hydrometeorology*. DOI 10.1175/JHM-D-20-0283.1.

updrafts, mostly around the temperature of the secondary Ze maximum. Overall, the median VR profiles are relatively constant against temperature for all three sites. We note that average VR at Blue Cow is less than over Cabramurra and Murray-1, suggesting that a mean upslope velocity is present at these two upwind sites. The Blue Cow VR profile shows consistent median values below -1.5 m s^{-1} which could indicate either downdrafts or falling precipitation (or both). Snow that grows as it falls under no vertical winds would produce relatively constant negative VR values at the terminal velocity with increasing Ze. The observed VR values are too strong for this scenario given that the snow's terminal velocity is about 0.5 m s^{-1}, which indicates that there is likely consistent downdraft over this site.

Compared to UF periods, hydrometeors at Cabramurra and Murray-1 are observed at lower temperatures during UP periods (Figure 4c), with Cabramurra showing an overall positive Ze slope and higher variability, which indicates larger hydrometers with altitude likely linked to convection at these colder temperatures. Cabramurra's median VR profile (Figure 4d) remains negative at all temperatures, although the standard deviation indicates that periods of updrafts are present but infrequent. The Murray-1 Ze profile is almost vertical with increased variability, while the median VR increases with increased height/decreased temperatures. Blue Cow again shows overall lower VR throughout the profile, likely due to orographic downdrafts and larger particles at the warmer temperatures. In contrast to UF, VR observations for all sites show a clear positive slope, which would indicate that the hydrometers' terminal velocity is increasing as it falls, this points to riming as a likely growth mechanism.

Similar Ze profiles are seen during the blocked frontal and post-frontal periods (BF & BP; Figures 4f & 4h), although during BF periods Ze is slightly higher overall, with less variability. Similar to the UP periods, an overall positive Ze slope is seen at Cabramurra

File generated with AMS Word template 1.0

during both blocked periods, with VR observations showing mostly negative values and positive slopes.

In a typical ice phase stratiform profile, reflectivity decreases with height, because ice particles grow by aggregation or vapor deposition as they fall, producing large particles and therefore higher reflectivities further down. The constant and even positively sloped Ze profiles observed (e.g. Figure 4h at Cabramurra) indicate that strong uplift, either by the orography or convection or both, brings bigger ice aggregates or snowflakes higher up which creates high reflectivity at lower temperatures. Meanwhile at warmer temperatures the lower observed reflectivities indicate a dominance of smaller hydrometeors (compared to convective conditions). This is not observed at Blue-Cow, which indicates the low likelihood of convective cells reaching this site.

In summary:

Convective precipitation is more likely in the windward slopes, especially during frontal periods.

Post-frontal precipitation is mostly stratiform, but there is evidence of large particles being uplifted upwind from the windward slopes.

Particle growth by riming is likely present during post-frontal periods, while vapor deposition and aggregation are likely dominant during frontal periods.

3.2.3 Frequency of occurrence of SLW at cloud-top

To explore any orographic effect on overpassing clouds as a function of synoptic and dynamic conditions, cloud-top phase data from the Himawari-8 satellite is shown in Figure 5 for the period between the first and last precipitation events (inclusive) including the non-precipitating times between events. These data were separated into the six subsets: UF, BF,

Accepted for publication in *Journal of Hydrometeorology*. DOI 10.1175/JHM-D-20-0283.1.

UP, BP, and unblocked and blocked periods with no precipitation. These cloud products and the algorithms used to produce them are detailed in Huang et al. (2019).

The periods with no precipitation show SLW cloud-tops above and immediately upwind of the mountain tops, but with reduced spatial extent (Figure 5e & 5f). This is especially evident during blocked conditions, which accounted for more than half the campaign's time and showed mostly clear skies.

During frontal periods (UF & BF, Figure 5a & b) the domain is dominated by clouds with glaciated tops, while during post-frontal periods (UP and BP, Figure 5c & d), SLW cloud-tops dominate areas associated with windward slopes and the mountain tops. Around the peak near Blue Cow, SLW occurrence frequencies reached up to 80% (not shown), which is consistent with a 5-year climatology of cloud-top phase derived from MODIS imagery (Morrison et al. 2011).

UP periods exhibited warm liquid cloud-tops far upwind from the ranges that transition to SLW cloud-tops. In contrast, mostly clear skies occur upwind and downwind from the ride axes when the post-frontal flow is blocked (BP), and a wide SLW band stretches much further south than during UP conditions. This would indicate that unlike the other three precipitation subsets, during BP periods there are few incoming clouds that get enhanced locally by the orography. Instead clouds are mostly created by the uplift over stagnated air before the barrier, creating mostly SLW clouds in the sub-freezing air at higher altitudes.

3.2.4 Orographic enhancement mechanisms

Out of the twelve mechanisms for orographic precipitation enhancement defined by Houze (2012), three mechanisms (Unblocked Stratiform Enhancement (USE), Orographic Convection Invigoration (OCI), and Blocked Stratiform Enhancement (BSE)) are likely

Accepted for publication in *Journal of Hydrometeorology*. DOI 10.1175/JHM-D-20-0283.1.

associated with most of the precipitation observed during the campaign. We disregarded eight of the twelve mechanisms that involve pronounced leeside precipitation given the low precipitation observed in downwind sites (sections 3.2.1 and 3.2.3). Another mechanism, related to diurnal forcing, can be discarded as no significant diurnal signature was observed in the high temporal resolution, 20-year dataset for the high-altitude sites, during winter.

Out of the three mechanisms, BSE is the only one to occur during blocked conditions. BSE moves the precipitation peak upwind, as the barrier is effectively extended upwind by the stagnant air mass, lifting incoming air earlier. This is observed in Figure 3 as these subsets (BF and BP) show more than half of their respective precipitation volumes falling in bins more than 12 km upwind from the ridge axis. The upwind offset of the precipitation enhancement is more pronounced during the frontal periods, compared to the post-frontal periods. This points to the added complexity resulting from the passage of the deep frontal cloud band and could explain the observed frequent updraft at Cabramurra during BF periods (Figure 4), which would not be expected from BSE.

Of the two remaining mechanisms, OCI would tend to enhance precipitation mostly along the windward slopes, with higher associated precipitation intensities, while USE would show lower intensities with precipitation occurring more towards the mountain tops. From this we would associate OCI with UF periods which show the highest mean precipitation intensities (Table 3) and more precipitation right at the upwind slopes (Figure 3). USE is likely accounting for most of the precipitation associated with UP periods, which show the highest precipitation right at the ridge axis (Figure 3) and have half the mean precipitation intensity than UF; yet is likely that OCI is also contributing in the upwind slope sites.

It should be noted that the analysis in section 3.2 is a composite from a six-week campaign; individual events may differ considerably. Nevertheless, evidence of some

commonality of these events is present. Processes that may be event-dependent will be investigated further in the two cases studies in Section 4, where other complementary observations, such as ground-based observations, will be analyzed in greater detail.

3.3 Precipitation characteristics at Cabramurra

Focusing on the relatively heavy precipitation common to the upwind slopes, observations from the additional instrumentation installed at Cabramurra is now explored. A summary of the meteorological conditions associated with each precipitation event through the field campaign is presented in Table 4. Of the ten events, seven events were embedded lows with fronts, which accounted for 62% of the precipitation by volume at Cabramurra. For these events, more precipitation (64%) was observed during post-frontal periods. For the three events classified as cut-off lows (accounting for 38% of the precipitation by volume) 54% of their precipitation occurred during post-frontal periods. Note that under prescribed meteorological conditions Snowy Hydro operates cloud seeding generators in the vicinity of the sites (Manton et al. 2017). We identified the events as seeded in Table 4 if, at any moment during the events, the generators were in operation. Any effects of cloud seeding on the microphysical processes are not examined here.

The total precipitation recorded by the Particle Size Velocity (PARSIVEL) optical disdrometer at Cabramurra was 344 mm for the campaign period, with ~70% in the form of snow, ~21% as rain, ~1% as freezing rain, and ~9% as mixed-phase precipitation. About three quarters of the snow was rimed. Details on the methodology used by the PARSIVEL for phase determination are presented in Supplemental Material Section 1. Segregating the precipitation between frontal and post-frontal periods (Figure 6), shows that post-frontal precipitation at Cabramurra is even more heavily favored (71%) than over all high-altitude Snowy Hydro sites (56.2%, Table 3). Although the mean precipitation intensity was higher

during the post-frontal periods (2.2 mm•h^{-1}) than the frontal periods (1.9 mm h^{-1}), the precipitation intensity statistical distributions were very similar with almost identical 25th, 50th, and 75th percentiles. The difference in the means is due to the extent of the post-frontal distribution's high tail; many of the intense precipitation events were observed in post-frontal conditions at Cabramurra. During post-frontal periods, precipitation was mostly (87%) snow, with 2% of the volume as freezing rain, 4% mixed and 7% as warm rain (Figure 7, left panel). In contrast, during frontal periods there was less snow (47%) and freezing rain (0%), and more warm rain (37%) and mixed phase (17%) (Figure 7, left panel).

Turning to the sensitivity of precipitation to upwind stability (Table 3) 81% of the precipitation at Cabramurra occurred during blocked conditions, primarily during the post-frontal periods (58%). This distribution was similar to the region-wide precipitation (Table 3) with the strongest contrast in the mean precipitation intensity observed during BF periods, which is consistent with the MRR analysis where deep convection is observed at Cabramurra during periods of local blocking.

The Particle Size Distribution (PSD) at Cabramurra was calculated from the PARSIVEL observations using the methodology described in Tokay et al. (2013) to calculate the sampling volume of each velocity bin. The PSD was plotted against particle diameter and segregated by phase (Figure 7, right panel). We found that the peak mean particle concentration occurred for particles with 0.6 mm diameter regardless of phase. At this diameter, freezing rain showed the highest particle concentration, while snow had the highest concentrations for larger diameters. Mixed phase precipitation was very close to rain, albeit slightly higher, indicating that the recorded mixed phase was likely dominated by rain.

Overall observations at Cabramurra show that most events lasted more than 1 day, with most of the precipitation reaching the ground after the frontal passage mainly in the form of

Accepted for publication in *Journal of Hydrometeorology*. DOI 10.1175/JHM-D-20-0283.1.

snow. Of the precipitation that occurred during the frontal passage, about half the volume was snow. Mixed phase precipitation was more frequent during frontal periods.

4 Case Studies

To better understand precipitation processes, events 2 and 3 are further examined here. These events are chosen because: (1) all key instruments were in operation, (2) relatively large amounts of precipitation were produced (Figure 6), and (3) the events were characterized by distinct synoptic settings and precipitation regimes. Specifically, Event 2 received the highest amount of frontal precipitation during the campaign and overall accumulated 30 mm of precipitation at Cabramurra. Event 3 had the second highest accumulated precipitation (68 mm) which was mostly post-frontal. We note that these two events are closely coupled, with event 3 beginning ~38 hours after the end of event 2.

Case Study 1. Frontal dominated event

Event 2 was associated with a cold front moving eastward at about 90 knots that was linked to a weak cut-off low (Figure 8 left). Although the entire event lasted about 27 hours, half of the precipitation occurred during the first 5 hours and therefore was classified as frontal. This event had relatively low post-frontal accumulated precipitation, likely due to: (1) the front moving relatively quickly allowing little time for post-frontal precipitation to develop; and (2) related to the first point, another front (Case Study 2) was following relatively closely which could diminish the available post-frontal moisture for this event. The event started on August 3rd at 04:21 (UTC) and ended on August 4th at 07:19 (UTC). The transition from frontal to post-frontal was observed on August 3rd at 13:20 (UTC). Radiosondes were launched on August 3rd at 00:00 (UTC) and on August 3rd at 12:00

Accepted for publication in *Journal of Hydrometeorology*. DOI 10.1175/JHM-D-20-0283.1.

(UTC). These soundings show no CAPE (Convective Available Potential Energy) and 0.03 s^{-1} wind shear between 3.4 and 3.6 km ASL (Figure 9a & 9b). A strong low-level inversion, likely the remnant of the nocturnal layer, was present in the first sonde profile, before the frontal period, with a relatively dry air mass above the surface. The second sonde profile, close to the end of the frontal period, shows a humid atmosphere up to 650 hPa, close to the moist adiabat. This event recorded the highest percentage of mixed phase precipitation at Cabramurra (38%) while having a relatively low percentage of snow (36%). The melting layer height was identified from sonde observations at ~2.1 km ASL prior to the event and lowered to ~1.7 km following the passage of the front. The source of the frontal and post-frontal air masses differed markedly, as evident in the 24 HYSPLIT back trajectories (Stein et al. 2015, Figure 9c & 9d) northerly flow advected towards the Snowy Mountains during frontal conditions, followed by a shift to a westerly post-frontal air mass, sourced over the Great Australian Bight, consistent with the climatological analysis of Chubb et al. (2011).

From the time series of radar reflectivity from the Bistatic Radar System for Atmospheric Studies (BASTA) and MRR instruments, as well as the cloud top height estimates from Himawari-8 (Figure 10a & 10b), about 4.5 km difference in cloud height between the frontal and post-frontal periods is evident. The temporal variability of the melting layer is also noted, as indicated by the bright band in the MRR Ze and abrupt vertical gradient in MRR Doppler velocity around 2km ASL (Figure 10b & 10c). During the frontal period, precipitation became evident from about 4 km ASL, intensified as it fell, and melted at around 2.2 km ASL. The abrupt lowering of the melting layer was detected as the cold frontal air mass reached the site. Until this point, most precipitation reached the ground as either warm rain or mixed-phase, according to PARSIVEL observations (Figure 10d). As the melting layer reached ground level, the PARSIVEL started to record precipitation that was dominated by

Accepted for publication in *Journal of Hydrometeorology*. DOI 10.1175/JHM-D-20-0283.1.

snow, from about 10:00 to 12:00 03-August. Afterwards, most of the precipitation was in the form of snow with some freezing rain towards the end of the post-frontal period. During the post-frontal period, precipitation was evident in the MRR observations up to about 2.6 km ASL.

Contoured Frequency by Temperature Diagrams (CFTDs) were created for selected periods (see dashed boxes in Figure 10) during the frontal and post-frontal parts of this event to compare Ze and VR observations from the three sites (Figure 11).

During the frontal period a similar radar reflectivity at the surface was observed for Cabramurra (~33 dBZe) and Murray-1 (~30 dBZe), while Blue Cow shows significantly lower values (~25 dBZe) presumably due to the site being above the melting layer.

Focusing on Ze at temperatures below 0 ˚C, the frequency profiles are similar to the respective subset (UF) in Figure 4. For this period, Himawari-8 shows ice at the cloud top over the whole domain. The highest degree of ice particle growth with respect to temperature is observed at Cabramurra; with an increase of ~1.25 dBZe per ˚C (Figure 11b). Here the Ze slope shows two distinct sections, between -10 to -7 ˚C, and between -7 and 0 ˚C. The colder section indicates increased particle growth and a very narrow VR distribution. This narrow VR distribution indicates that this section is dominated by a single growth process as different microphysical processes have different growth rates, leading to a broadening of the VR distribution. The closest radiosondes (Figure 9b) show a fully saturated atmosphere up to -15 ˚C, which would favor particle growth by vapor deposition (Houze 2014). The dominance of growth by vapor deposition close to the top of the windward slope is consistent with findings in Saleeby et al (2013) based on modelling work. The warmer section, at temperatures above -7 ˚C, has a relatively slower growth rate and a larger VR spread. Here, the increase in VR as particles descend is most likely accounted for by aggregation (Houze

File generated with AMS Word template 1.0

2014). We infer that the observed particle growth is likely driven by vapor deposition aloft, with most of the observed growth favoring prism-like ice habits (Kuroda and Lacmann 1982), which then are aggregated between -7 to 0 ˚C. This same pattern is observed in Murray-1. Blue Cow's Ze profile shows particle growth between -15 and -7 ˚C, likely via vapor deposition, but no growth between -7 and 0 ˚C. In addition, the VR observations for the whole profile are consistent at ~-1.5 m s^{-1}.

During the post-frontal period, much shallower precipitation was observed, with the vertical extents of the precipitation profiles of approximately 1.6 km, 0.9 km and 1.3 km at Murray-1, Cabramurra and Blue Cow, respectively. The highest particle growth with temperature also occurs at Cabramurra (~2.5 dBZe per ˚C, Figure 11h), a factor of two greater than that during the frontal period. In this case the temperature range is between -6 to 0 ˚C and there is a clear decrease in VR as well as broadening of the distribution (with temperature). Since the melting layer was below the site during this period, PARSIVEL observations can be used to identify the types of hydrometeors present. About three quarters of the solid precipitation during this period were estimated to be rimed snow. Indeed, Himawari-8 shows SLW cloud-top over most of the domain instead of ice during this period of time, indicating a favorable environment for particle growth by riming, which likely accounted for the higher Ze slope.

The event's frontal period shown in Figure 11 (a-f) falls in the UF subset, where, according to the climatology, OCI would have likely been the dominant mechanism by which the orography interacts with the overpassing clouds. An increase of about 5 dBZe is clearly observed at Cabramurra compared to Murray-1 throughout the profile. Conversely, Blue Cow shows higher reflectivities aloft but lower particle growth than Cabramurra. Nevertheless, OCI would be associated with updrafts at Murray-1 and Cabramurra, which are rarely present

Accepted for publication in *Journal of Hydrometeorology*. DOI 10.1175/JHM-D-20-0283.1.

in figure 10c. This would indicate that for this specific event, OCI was likely not dominant during the UF period. Based on the low precipitation intensity and low frequency of updrafts, this precipitation is likely more stratiform in nature, and shows a clear orographic enhancement in Figure 11a-c; which points to USE as the dominant mechanism.

Case Study 2. Post-frontal dominated event

Event 3 was the result of a cold front moving eastward at about 40 knots associated with an embedded low (Figure 8 right). The event started on August 5th at 21:30 (UTC) and ended on August 7th at 07:10. The transition from frontal to post-frontal was observed on August 6th at 01:50 (Figure 13). Sondes were launched approximately every 3 hours (with some interim soundings) through the event, and a tropopause fold is evident (Figure 12c). At Cabramurra, this event was almost entirely snow (99%) with ~ 27% in the form of un-rimed snow and ~ 72% as rimed snow.

A spike in precipitation is observed during the passage of the front (Figure 13d); this is followed by low precipitation for several hours, after which a prolonged period of high-intensity intermittent precipitation with frequent updrafts occurred. A period of sustained but mild intensity precipitation follows which shows fewer and weaker updrafts. Consequently, this event was not only divided into frontal and post-frontal (on August 6th at 01:50), but the post-frontal period was further sub-divided into a convective period and a stratiform period (on August 6th at 18:00).

During frontal conditions, a deep cloud band up to 7.5 km ASL is shown by the BASTA observations, while precipitation became evident in the MRR below about 3.5 km ASL. Although relatively intense, this precipitation was short lived and only accounted for 3% of the event's total precipitation volume. The melting layer height was at about 1.2 km ASL (Figure 12a) and a small CAPE of 61 $J \bullet kg^{-1}$ is observed. There is a weak inversion at 3 km

ASL and the air mass is close to saturation between 2 km and 6 km ASL. A wind shear of 0.04 s^{-1} was also observed between 4.5 km and 4.7 km ASL. The back trajectory (Figure 12d), as in the previous case study, shows the source of the air mass coming from the North of the region during the frontal passage, traversing less distance than during the first case study.

The post-frontal convective period that dominated the first 13 post-frontal hours was characterized by optically thick, high-top clouds (Figure 13a) that produced short periods of intense precipitation at the surface (Figure 13d). 57% of the post-frontal precipitation occurred during this period. Soundings during the convective period show a significant CAPE of 415.9 $J \bullet kg^{-1}$ with a strong inversion at 6 km ASL (Figure 13b). This is consistent with BASTA observations, which show clouds corresponding to this period present up to 6.8 km ASL (Figure 13a). Frequent updrafts can be observed (Figure 13c) during this period in the VR data.

During the post-frontal stratiform period, shallower clouds with sustained precipitation, but with lower intensities, were observed (Figure 13a) and accounted for 43% of the event's total post-frontal precipitation. Soundings show no CAPE and an atmosphere following approximately the moist adiabat up to the inversion at 6 km ASL (Figure 12c). There are still updrafts present in the VR observations (Figure 13c), but these are less frequent and milder compared to the convective period.

Back trajectories during these periods (Figure 12e & 12f) suggest slightly different sources of the air mass, with the convective period's air mass residing over land during most of the previous 24 hours, while the stratiform period's air mass resides over the Southern Ocean half of this time. The origin of the stratiform air mass might partially explain the larger humidity present in this period's soundings.

Accepted for publication in *Journal of Hydrometeorology*. DOI 10.1175/JHM-D-20-0283.1.

In order to examine the vertical structure of the precipitation profiles, equal time sections from each period were selected with homogeneous precipitation signatures, and CFTDs of Ze and VR were created from MRR observations (Figure 14). From these CFTDs, stronger radar reflectivity was recorded during the convective period compared to the stratiform period, indicating the vertical extent of the intense precipitation. The stratiform period shows a smaller vertical extent but a larger Ze slope with respect to temperature than the convective period. Looking at the VR CFTDs, there is a pronounced updraft component during the convective period (Figure 14d-f), mostly dominating below -10 ˚C, whereas the stratiform period was characterized by mild, and fairly consistent, downward VR primarily in the range of 0 to 2 m s^{-1} (Figure 14j-l). During the stratiform period at Cabramurra (Figure 14k), collocated PARSIVEL observations at the surface estimated that about 67% of the snow was rimed. During the convective period, the presence of strong updraft components and the variability of VR make it more challenging to infer the hydrometeor type. It is, however, evident that there is likely hydrometeor growth with increasing temperature (decreasing altitude) as suggested by the overall increase in Ze and fall speed with decreased altitude. During this period, the PARSIVEL estimated 74% of the snow was rimed.

It is likely that $\hat{H}^2$ is the driving factor behind the differences between these two post-frontal periods. In Figure 13, it is noted that the transition from convective to stratiform coincides with a transition from unblocked to blocked. In the unblocked scenario, the wind flow typically ascends over the mountains with no upstream deceleration, resulting in pronounced upward motions; in the blocked scenario, the upstream deceleration forms, which often results in reduced upward velocity along the upslope of the mountain.

The event's stratiform period agrees well with BSE predictions, with relatively mild intensity precipitation occurring in Cabramurra and Blue Cow, and little presence of updrafts.

Accepted for publication in *Journal of Hydrometeorology*. DOI 10.1175/JHM-D-20-0283.1.

On the other hand, the convective period falls under the UP subset, which should favor USE yet Figure 14 suggests that it is likely that OCI is the driving mechanism in this instance. This would explain the higher variability observed in Figure 4c and would indicate that OCI is partly occurring during UP periods.

5 Conclusions

An intense field campaign was carried out over the Snowy Mountains, in the south-eastern region of Australia, to characterize the dynamic and microphysical mechanisms driving winter precipitation in this area. The 44-day campaign in winter 2018 deployed a vertically pointing micro rain radar, cloud radar, lidar, radiometer, and PARSIVEL disdrometer, among other instruments at a main study site at Cabramurra (1,502 m ASL). There were two support sites (337 and 1,902 m ASL) with vertically-pointing micro rain radars. An existing network of 76 pluviometer distributed across the mountains was also used. The synoptic environment was broken into four classes: unblocked frontal (UF), blocked frontal (BF), unblocked post-frontal (UP) and blocked post-frontal (BP) with blocking referring to local (orographic) stability.

- Most precipitation occurred on windward slopes and high-altitude sites

Total accumulated precipitation in the pluviometer network exhibited a strong enhancement in the windward slopes sites (~38%) and high-altitude sites (~54%), with very little precipitation observed in the leeside sites of the mountain (~9%). All precipitation events were associated with the passage of cold fronts. While these fronts drove the

Accepted for publication in *Journal of Hydrometeorology*. DOI 10.1175/JHM-D-20-0283.1.

precipitation events, only about half (47%) of the domain-wide precipitation occurred during the frontal passage, with the rest occurring in the post-frontal environment.

Two thirds of the frontal precipitation (32% of total domain-wide accumulation) occurred during blocked conditions, which were generally stratiform in nature with fully glaciated cloud tops and relatively higher accumulations of precipitation farther upwind. The rest of the frontal precipitation (16% of total domain-wide accumulation) was also associated with fully glaciated cloud tops, but was more convective in nature, and tended to accumulate precipitation over the windward slopes. On the other hand, post-frontal periods favored accumulation over the mountain tops. This spatial distribution of frontal and post-frontal precipitation in the region was not investigated before.

- Blocked post-frontal periods had Supercooled Liquid Water (SLW) cloud tops over the high-altitude areas of the mountain over 80% of the time.

79% of the post-frontal precipitation occurred during blocked conditions. This precipitation resulted as the approaching cloudless air mass was lifted over stagnant air, upwind from the barrier, creating SLW clouds that produced mostly stratiform precipitation. The post-frontal precipitation that fell during unblocked conditions was likely generally stratiform and mostly over the mountain tops, but there is evidence of periods of convective enhancement mostly occurring over the windward slopes. Previous studies reported SLW frequencies between 40-50% of the time in winter in these mountains, but the synoptic (frontal / post-frontal) and dynamic (blocked / unblocked) segregation done in the present study shows that the SLW frequency can be as high as 80% over the mountain tops during BP conditions.

Accepted for publication in *Journal of Hydrometeorology*. DOI 10.1175/JHM-D-20-0283.1.

- Blocked Stratiform Enhancement (BSE) was the orographic mechanism associated with most of the accumulated precipitation.

Two precipitation events were examined in detail and mostly confirmed that BSE is the dominant orographic mechanism during blocked conditions, and is associated with most of the accumulated precipitation. While the characteristics of UF precipitation were consistent with the proposed OCI mechanism, updrafts were not observed at the windward slope sites. From the campaign-wide analysis of UP periods, the orographic mechanism that would seem most dominant was USE, yet the second case study showed that OCI can also drive precipitation in these periods.

- New insights on the dominant hydrometer types over the Snowy Mountains were obtained from disdrometer observations at Cabramurra.

During frontal periods particle growth is likely dominated by vapor deposition at temperatures below -7 ˚C, with aggregation contributing between -7 ˚C and 0 ˚C. Mixed phase represented the highest accumulation by type during unblocked flows, while rain had the highest accumulation during blocked flows.

During post-frontal periods hydrometeors tended to be more heterogeneous, with about two thirds of the snow falling as rimed particles at the ground. Rimed snow dominated both post-frontal subsets. Freezing rain was almost exclusively recorded during BP periods with all other subsets recording minimal accumulations. All periods recorded some rain and mixed phase accumulations except for UP, which saw virtually only rimed and un-rimed snow.

Accepted for publication in *Journal of Hydrometeorology*. DOI 10.1175/JHM-D-20-0283.1.

Further studies using numerical modeling are necessary to extend these limited observations. The models need to be able to simulate SLW and the link with low-level air flow. Specifically, simulations may provide greater insight into the interaction between the local dynamics, the generation of supercooled liquid water and the formation of precipitation. The observation that SLW clouds are most likely to occur during blocked conditions is of particular relevance to cloud seeding activities, because the vertical mixing of seeding material from ground-based generators is limited in these conditions. The campaign's dataset is made available as a benchmark for future modeling studies to be evaluated in this region; with a large suit of measurements to compare the models' results, this can also help improve quantitative precipitation forecast.

Acknowledgments.

This research has been supported by ARC Linkage Grant LP160101494. Luis Ackermann is supported by the Monash Graduate Scholarship. We thank Snowy Hydro Limited for providing pluviometer data for the Snowy Mountains, Dr. Hamish McGowan for lending a Micro Rain Radar used in this campaign and Brad Atkinson for his technical help. We also want to thank the reviewers whose expert insights greatly improved the hydrometer type classification.

Data Availability Statement.

Most of the data used in this study and the source code used to generate all figures and tables are openly available at Monash University Data Repository. The project database can be accessed at https://bridges.monash.edu/projects/Snowy_Mountains_Winter

_Observation_Campaign_2018/93239. Due to the large size of the Micro Rain Radar dataset (>31 GB) and size limitations from the university's data repository, the Micro Rain Radar dataset is available from Steven Siems (steven.siems@monash.edu) at Monash University. Due to confidentiality agreements with Snowy Hydro Limited, the exact location of each pluviometer cannot be made openly available. The pluviometer data is available at the project database with general location labels but without latitude/longitude coordinates. Exact coordinates can be provided to bona fide researchers subject to a non-disclosure agreement with Snowy Hydro Limited. For more information contact Steven Siems (steven.siems@monash.edu) at Monash University. Cloud products from Himawari-8 used in section 3.2.3 are disseminated by the Australian Bureau of Meteorology and can be directly obtained from Australia's National Computational Infrastructure (NCI) servers following registration.

REFERENCES

Ades, M., and Coauthors, 2019: State of the climate in 2018. Bull. Am. Meteorol. Soc., https://doi.org/10.1175/2019BAMSStateoftheClimate.1.

Australian Bureau Of Meteorology, 2018: Special Climate Statement 66 — an abnormally dry period in eastern Australia. 1–31.

Chubb, T., M. J. Manton, S. T. Siems, A. D. Peace, and S. P. Bilish, 2015: Estimation of Wind-Induced Losses from a Precipitation Gauge Network in the Australian Snowy Mountains. J. Hydrometeorol., 16, 2619–2639, https://doi.org/10.1175/JHM-D-14-0216.1.

Chubb, T., Y. Huang, J. Jensen, T. Campos, S. Siems, and M. Manton, 2016a: Observations of high droplet number concentrations in Southern Ocean boundary layer clouds. Atmos. Chem. Phys., 16, https://doi.org/10.5194/acp-16-971-2016.

Chubb, T., M. Manton, S. Siems, and A. Peace, 2016b: Evaluation of the AWAP daily precipitation spatial analysis with an independent gauge network in the Snowy Mountains. J. South. Hemisph. Earth Syst. Sci., 66, 55–67, https://doi.org/10.22499/3.6601.006.

Chubb, T. H., S. T. Siems, and M. J. Manton, 2011: On the Decline of Wintertime Precipitation in the Snowy Mountains of Southeastern Australia. J. Hydrometeorol., 12, 1483–1497, https://doi.org/10.1175/JHM-D-10-05021.1.

——, J. B. Jensen, S. T. Siems, and M. J. Manton, 2013: In situ observations of supercooled liquid clouds over the Southern Ocean during the HIAPER Pole-to-Pole Observation campaigns. Geophys. Res. Lett., https://doi.org/10.1002/grl.50986.

French, J. R., and Coauthors, 2018: Precipitation formation from orographic cloud seeding. Proc. Natl. Acad. Sci. U. S. A., 115, 1168–1173, https://doi.org/10.1073/pnas.1716995115.

Hersbach, H., and Coauthors, 2020: The ERA5 global reanalysis. Q. J. R. Meteorol. Soc., https://doi.org/10.1002/qj.3803.

Hindman, E. E. (1986). Characteristics of Supercooled Liquid Water in Clouds at Mountaintop Sites in the Colorado Rockies. Journal of Climate and Applied Meteorology, 25(9), 1271-1279. https://doi.org/10.1175/1520-0450(1986)025<1271:COSLWI>2.0.CO;2

Accepted for publication in *Journal of Hydrometeorology*. DOI10.1175/JHM-D-20-0283.1.

Houze, R. A., 2012: Orographic effects on precipitating clouds. Rev. Geophys., 50, 1–47, https://doi.org/10.1029/2011RG000365.

——, 2014: Cloud microphysics. Cloud Dynamics, Vol. 104 of, 47–76.

Huang, Y. I., S. Siems, M. Manton, A. Protat, L. Majewski, and H. Nguyen, 2019: Evaluating himawari-8 cloud products using shipborne and CALIPSO observations: Cloud-top height and cloud-top temperature. J. Atmos. Ocean. Technol., 36, https://doi.org/10.1175/JTECH-D-18-0231.1.

Jones, D. A., W. Wang, and R. Fawcett, 2009: High-quality spatial climate data-sets for Australia. Aust. Meteorol. Oceanogr. J., https://doi.org/10.22499/2.5804.003.

Kuroda, T., and R. Lacmann, 1982: Growth kinetics of ice from the vapour phase and its growth forms. J. Cryst. Growth, https://doi.org/10.1016/0022-0248(82)90028-8.

Manton, M. J., and L. Warren, 2011: A confirmatory snowfall enhancement project in the snowy mountains of Australia. Part II: Primary and associated analyses. J. Appl. Meteorol. Climatol., https://doi.org/10.1175/2011JAMC2660.1.

——, ——, S. L. Kenyon, A. D. Peace, S. P. Bilish, and K. Kemsley, 2011: A confirmatory snowfall enhancement project in the snowy mountains of Australia. Part I: Project design and response variables. J. Appl. Meteorol. Climatol., https://doi.org/10.1175/2011JAMC2659.1.

——, A. D. Peace, K. Kemsley, S. Kenyon, J. C. Speirs, L. Warren, and J. Denholm, 2017: Further analysis of a snowfall enhancement project in the Snowy Mountains of Australia. Atmos. Res., 193, https://doi.org/10.1016/j.atmosres.2017.04.011.

Miller, S. D., T. L. Schmit, C. J. Seaman, D. T. Lindsey, M. M. Gunshor, R. A. Kohrs, Y. Sumida, and D. Hillger, 2016: A sight for sore eyes: The return of true color to

Accepted for publication in *Journal of Hydrometeorology*. DOI 10.1175/JHM-D-20-0283.1.

geostationary satellites. Bull. Am. Meteorol. Soc., https://doi.org/10.1175/BAMS-D-15-00154.1.

Minder, J. R., T. W. Letcher, L. S. Campbell, P. G. Veals, and W. J. Steenburgh, 2015: The Evolution of Lake-Effect Convection during Landfall and Orographic Uplift as Observed by Profiling Radars. Mon. Weather Rev., 143, 4422–4442, https://doi.org/10.1175/MWR-D-15-0117.1.

Morrison, A. E., S. T. Siems, and M. J. Manton, 2011: A three-year climatology of cloud-top phase over the Southern Ocean and North Pacific. J. Clim., https://doi.org/10.1175/2010JCLI3842.1.

——, ——, and ——, 2013: On a natural environment for glaciogenic cloud seeding. J. Appl. Meteorol. Climatol., 52, 1097–1104, https://doi.org/10.1175/JAMC-D-12-0108.1.

Murphy, B. F., and B. Timbal, 2008: A review of recent climate variability and climate change in Southeastern Australia. Int. J. Climatol., https://doi.org/10.1002/joc.1627.

Murray-Darling Basin Authority, 2017: Murray-Darling Basin Authority Annual Report 2017–18. 203 pp.

Nicholls, N., 2005: Climate variability, climate change and the Australian snow season. Aust. Meteorol. Mag.,.

Osburn, L., T. Chubb, S. Siems, M. Manton, and A. D. Peace, 2016: Observations of Supercooled Liquid Water in Wintertime Alpine Storms in South Eastern Australia. Atmos. Res., 169, 345–356, https://doi.org/10.1016/j.atmosres.2015.10.007.

Pook, M. J., P. C. McIntosh, and G. A. Meyers, 2006: The synoptic decomposition of cool-season rainfall in the southeastern Australian cropping region. J. Appl. Meteorol. Climatol., https://doi.org/10.1175/JAM2394.1.

Ryan, B. F., and K. J. Wilson, 1984: The Australian summertime cool change. Part III: Subsynoptic and mesoscale model. Mon. Weather Rev., 113, 224–240.

Saleeby, S. M., Cotton, W. R., Lowenthal, D., & Messina, J. (2013). Aerosol Impacts on the Microphysical Growth Processes of Orographic Snowfall. Journal of Applied Meteorology and Climatology, 52(4), 834-852. https://doi.org/10.1175/JAMC-D-12-0193.1

Sarmadi, F., Y. Huang, S. T. Siems, and M. J. Manton, 2017: Characteristics of Wintertime Daily Precipitation over the Australian Snowy Mountains. J. Hydrometeorol., 18, 2849–2867, https://doi.org/10.1175/JHM-D-17-0072.1.

——, ——, G. Thompson, S. T. Siems, and M. J. Manton, 2019: Simulations of orographic precipitation in the Snowy Mountains of Southeastern Australia. Atmos. Res., 219, https://doi.org/10.1016/j.atmosres.2019.01.002.

Simmonds, I., and K. Keay, 2000: Mean southern hemisphere extratropical cyclone behavior in the 40-year NCEP-NCAR reanalysis. J. Clim., 13, 873–885, https://doi.org/10.1175/1520-0442(2000)013<0873:MSHECB>2.0.CO;2.

Smith, R. B., 1980: Linear theory of stratified hydrostatic flow past an isolated mountain. Tellus, https://doi.org/10.3402/tellusa.v32i4.10590.

Stein, A. F., R. R. Draxler, G. D. Rolph, B. J. B. Stunder, M. D. Cohen, and F. Ngan, 2015: Noaa's hysplit atmospheric transport and dispersion modeling system. Bull. Am. Meteorol. Soc., https://doi.org/10.1175/BAMS-D-14-00110.1.

Stoelinga, M. T., and Coauthors, 2003: Improvement of microphysical parameterization through observational verification experiment. Bull. Am. Meteorol. Soc., https://doi.org/10.1175/BAMS-84-12-1807.

Accepted for publication in *Journal of Hydrometeorology*. DOI 10.1175/JHM-D-20-0283.1.

Theobald, A., H. McGowan, J. Speirs, and N. Callow, 2015: A synoptic classification of inflow-generating precipitation in the Snowy Mountains, Australia. J. Appl. Meteorol. Climatol., https://doi.org/10.1175/JAMC-D-14-0278.1.

Timbal, B., 2009: The continuing decline in South-East Australian rainfall - Update to May 2009. CAWCR Res. Lett., Issue 2, 4–12.

Tokay, A., W. A. Petersen, P. Gatlin, and M. Wingo, 2013: Comparison of raindrop size distribution measurements by collocated disdrometers. J. Atmos. Ocean. Technol., 30, 1672–1690, https://doi.org/10.1175/JTECH-D-12-00163.1.

Accepted for publication in *Journal of Hydrometeorology*. DOI 10.1175/JHM-D-20-0283.1.

TABLES

Table 1: Instruments deployed in the field campaign with a short description of measurement characteristics.

Measurement	**Instruments**	**Site**
Vertical profiles of radar reflectivity and Doppler velocity	24 GHz Micro Rain Radar (MRR)	Cabramurra, Murray-1, Blue Cow
	95 GHz Doppler Radar (Cloud radar, BASTA)	Cabramurra
Vertical profiles of elastic backscatter, depolarization ratio and Raman backscatter.	355 nm Raman LIDAR	Cabramurra
Vertical profiles of air temperature and humidity	Radiosondes	Murray-1 vicinity
	Multichannel Microwave Radiometer	Cabramurra
Water vapor column	Microwave Radiometer	Blue Cow
Particle morphology, size, fall speed, and distribution	PARSIVEL Disdrometer	Cabramurra
	2D precipitation imaging probe (PIP)	Cabramurra
	Holographic Microscope	Cabramurra
Standard weather station measurements	Various instruments measuring surface temperature, relative humidity, precipitation intensity, wind direction and speed.	Cabramurra, Blue Cow, 50 surface stations and 70 pluviometers across Snowy Mountains.

Table 2: Winter (May-October) precipitation climatology of seven high altitude sites.

Station Name	**Elevation (m)**	**1995-2015 mean winter precipitation (mm)**	**2018 winter precipitation (mm)**	**(2018 – mean) ÷ mean (%)**
Tooma Dam	1222	1157	840	-27
Geehi Dam	1161	1055	731	-31
Jagungal	1669	1104	489	-56
The Kerries	1741	1027	279	-73
Guthega Dam	1586	882	599	-32
Guthega PS	1321	963	368	-62
Cabramurra	1473	858	669	-22
Mean	**1453**	**1007**	**568**	**-43**

Accepted for publication in *Journal of Hydrometeorology*. DOI 10.1175/JHM-D-20-0283.1.

Table 3: Precipitation accumulation and mean intensity at the Snowy Mountains for the pluviometer sites and Cabramurra under different stability and frontal passage periods.

Location/Sites subset	**Frontal**	**Post-frontal**
SHL total mean precipitation	87 mm (47 %)	99 mm (53 %)
SHL Unblocked precipitation	16 % (1.5 mm hr^{-1})	10 % (0.7 mm hr^{-1})
SHL Blocked precipitation	32 % (0.7 mm hr^{-1})	42 % (0.3 mm hr^{-1})
Upwind sites mean precipitation (mean elevation 617m ASL)	92 mm (21 %)	76 mm (17 %)
High-altitude sites mean precipitation (mean elevation 1497m ASL)	104 mm (24 %)	133 mm (30 %)
Downwind sites mean precipitation (mean elevation 1143m ASL)	20 mm (5 %)	16 mm (4 %)
Cabramurra total mean precipitation	98 mm (29 %)	246 mm (71 %)
Cabramurra Unblocked precipitation	8 % (2.3 mm hr^{-1})	11 % (3.5 mm hr^{-1})
Cabramurra Blocked precipitation	23 % (1.8 mm hr^{-1})	58 % (2.1 mm hr^{-1})
Cabramurra mean SLW integrated column	0.048 mm	0.052 mm
Cabramurra mean surface temperature	3.0 C	0.9 C
Cabramurra mean cloud base height (ASL)	2162 m	1691 m
Cabramurra mean cloud top height (ASL)	5597 m	4361 m

Accepted for publication in *Journal of Hydrometeorology*. DOI10.1175/JHM-D-20-0283.1.

Table 4: Summary of precipitation events at Cabramurra during the field campaign.

Event #	Period start, stop [UTC]	Synoptic State	Total Precipitation [mm]	Frontal [%]	Post-Frontal [%]	seeded
1	Jul-28 08:40, Jul-29 23:16	Embedded low with front	22.5	15.8	84.2	No
2	Aug-03 04:21, Aug-04 07:19	Cut-off low with front	30	74.2	25.8	No
3	Aug-05 21:35, Aug-07 07:04	Embedded low with front	68.4	3	97	Yes
4	Aug-07 20:20, Aug-08 17:38	Embedded low with front	16.9	0.9	99.1	Yes
5	Aug-10 20:00, Aug-13 08:20	Embedded low with front	45.8	21	79	Yes
6	Aug-15 00:00, Aug-15 23:00	Embedded low with front	9.2	7.7	92.3	No
7	Aug-17 17:00, Aug-19 12:00	Cut-off low with front	79.9	22.7	77.3	Yes
8	Aug-20 12:00, Aug-21 23:00	Embedded low with front	13.5	32.7	67.3	Yes
9	Aug-30 20:30, Sep-01 09:30	Cut-off low with front	19.7	56	44	No
10	Sep-05 19:00, Sep-07 00:00	Embedded low with front	38	70	30	No

Accepted for publication in *Journal of Hydrometeorology*. DOI 10.1175/JHM-D-20-0283.1.

FIGURES

Figure 1: Campaign sites (red-outlined boxes) and pluviometer stations (dots colored by category as shown on legend). Black arrow shows predominant winds. Yellow stars show relevant cities for reference. Topography contour lines at 500, 1200, and 1700 m ASL. The yellow dashed line shows the overall ridge axis. Micro Rain Radars (MRR) were located at each campaign site. Blue Cow had an additional Radiometer. Cabramurra was the main site, which also housed a Cloud Radar and a PARSIVEL disdrometer among other instruments (see Table 1).

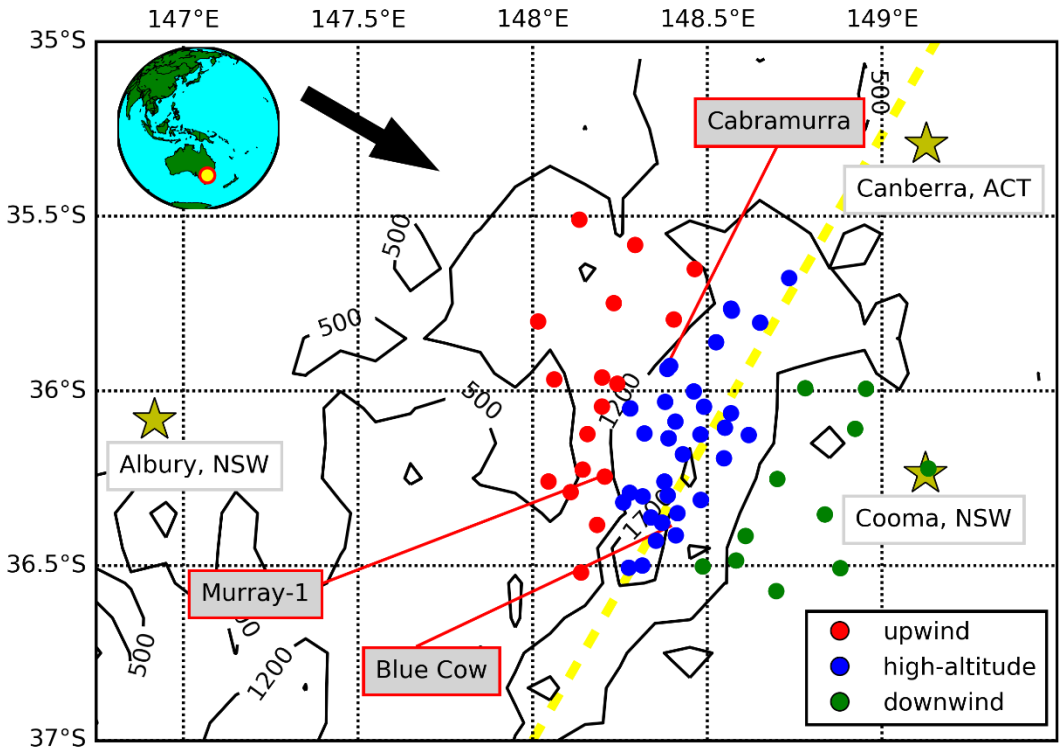

Accepted for publication in *Journal of Hydrometeorology*. DOI 10.1175/JHM-D-20-0283.1.

Figure 2: Precipitation accumulation at pluviometer sites. A) Only during frontal periods. B) Only during post-frontal periods. C) Total accumulation regardless of period. D) Difference between frontal and post-frontal precipitation accumulation. Contour lines show topography at 1.2 km ASL.

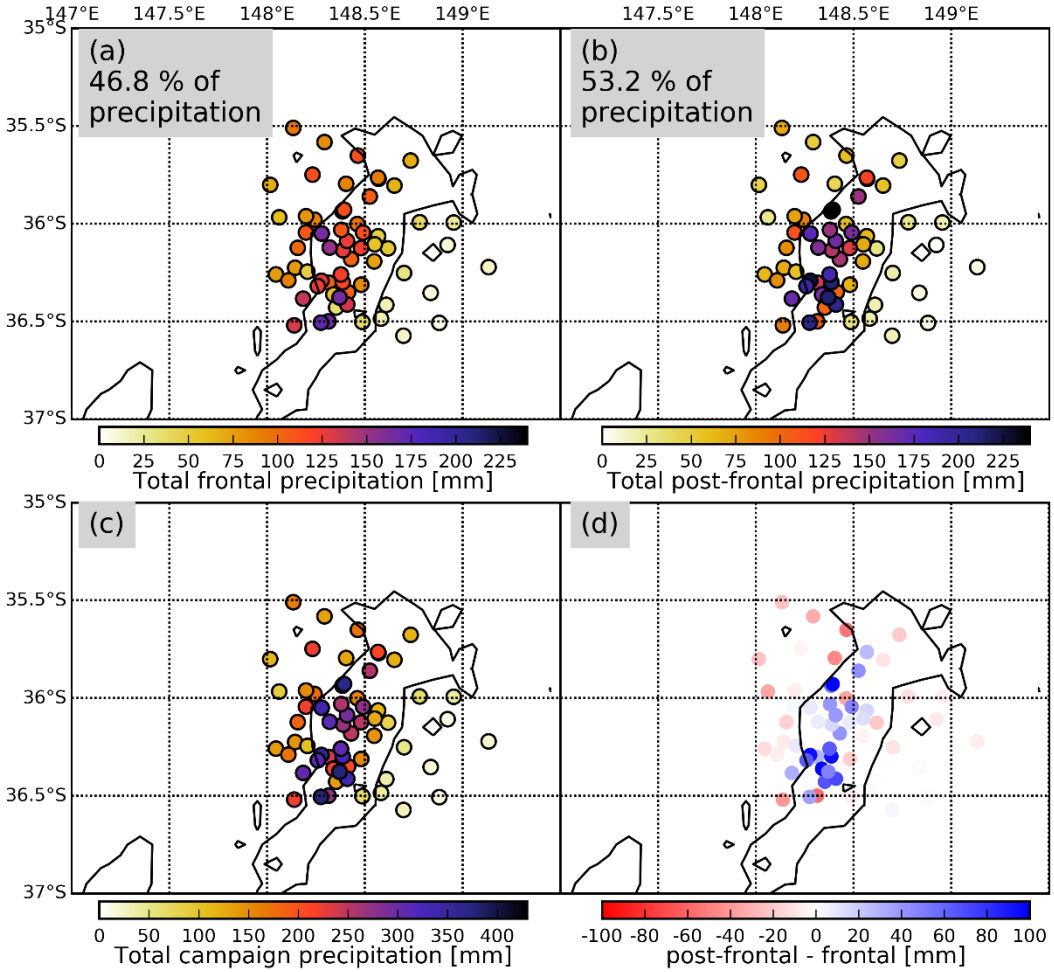

File generated with AMS Word template 1.0

Accepted for publication in *Journal of Hydrometeorology*. DOI 10.1175/JHM-D-20-0283.1.

Figure 3: Lines show mean precipitation with respect to distance from the ridge axes binned into 12 km increments (starting from the most upwind pluviometer). Shaded area shows the mean height of the sites in each 12 km bin. The green line shows all precipitation while UF, BF, UP, and BP shows only mean precipitation for unblocked & frontal, blocked & frontal, unblocked & post-frontal, and blocked & post-frontal periods, respectively. Negative x-axis values represent upwind sites.

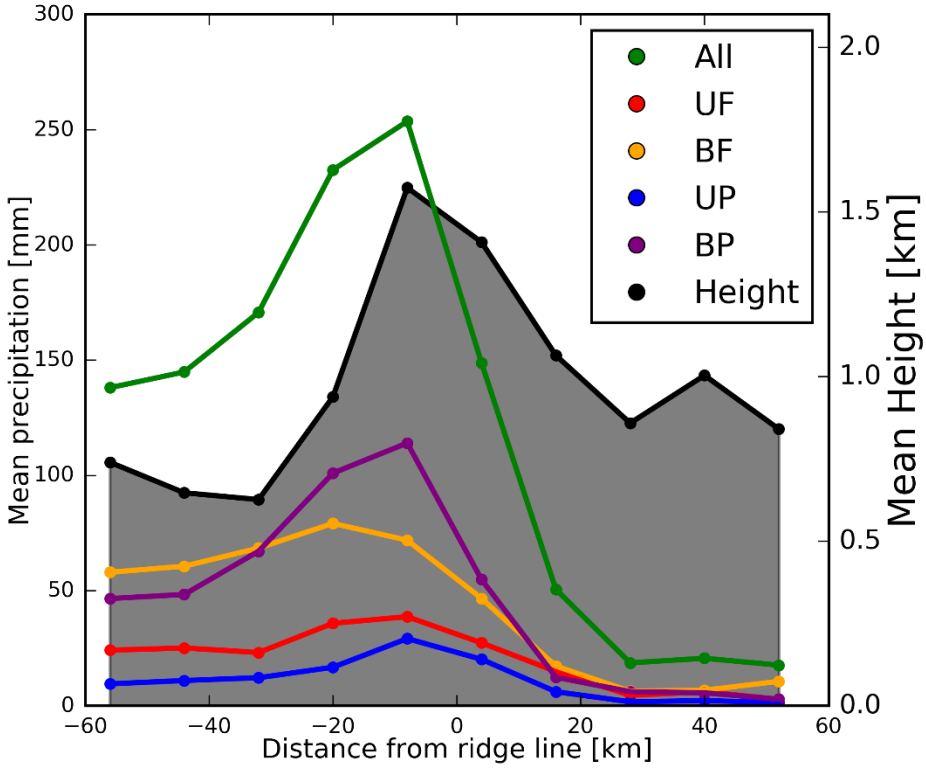

File generated with AMS Word template 1.0

Figure 4: Median radar reflectivity (dBZe) and Radial Velocity (VR) from MRRs with respect to temperature (from reanalysis) for each station segregated into: (A & B) frontal & unblocked. (C & D) post-frontal & unblocked. (F & G) frontal & blocked. (H & I) post-frontal & blocked. The shaded areas show ± 1 standard deviation. Only temperature bins for which at least 90 (for Murray-1 and Blue Cow) or 315 observations (for Cabramurra) where recorded are shown. The different data availability thresholds are due to the higher vertical resolution of the MRR at Cabramurra.

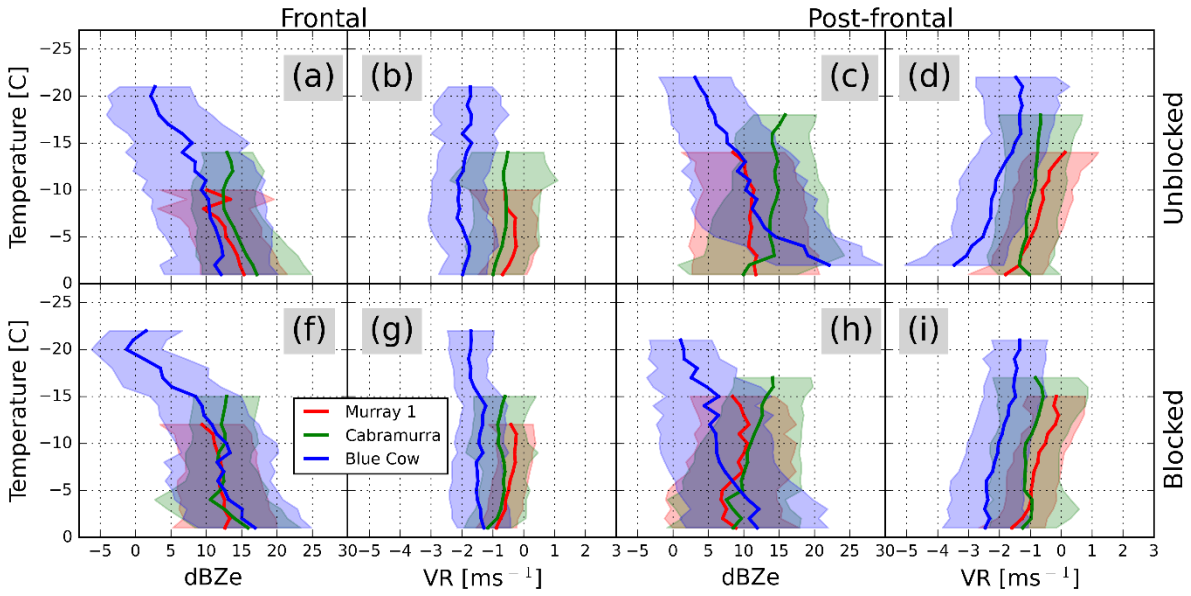

Accepted for publication in *Journal of Hydrometeorology*. DOI10.1175/JHM-D-20-0283.1.

Figure 5: Most frequent cloud-top phase observations by Himawari-8. Black contour shows topography at 1.2 km ASL. In panel B, the red and green contours show topography at 0.6 and 1.8 km ASL respectively. Times and percentages in each panel represent total fraction of the data for each period.

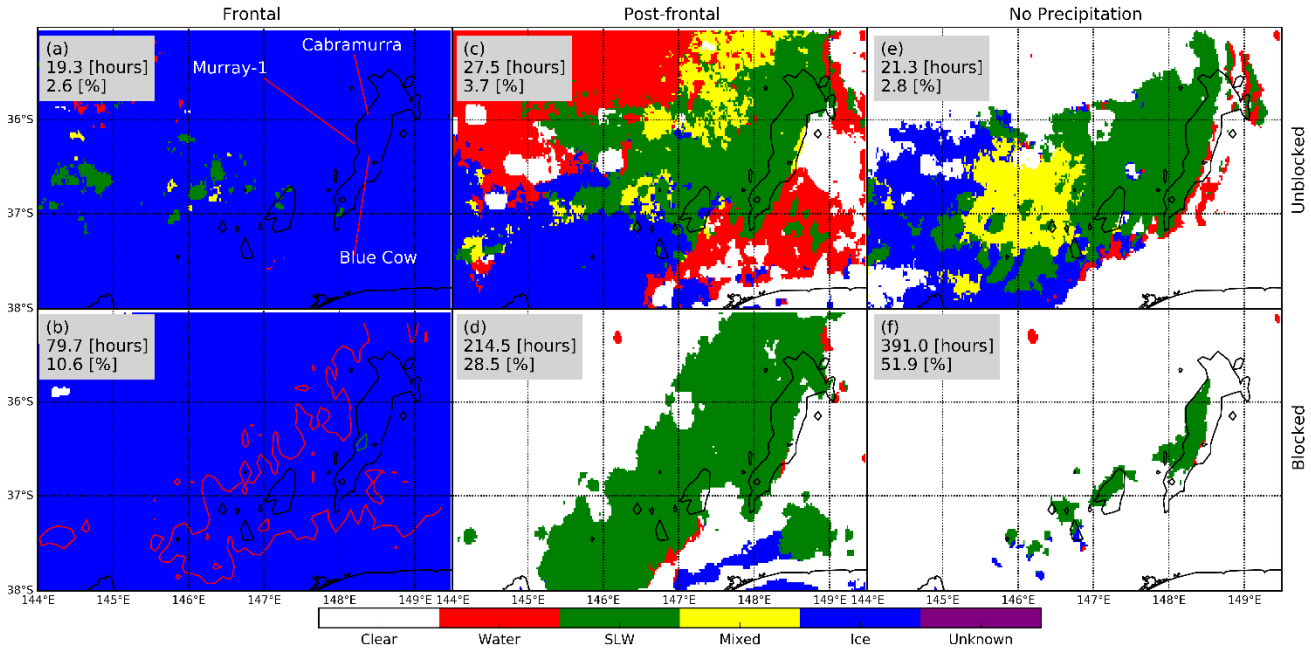

File generated with AMS Word template 1.0

Accepted for publication in *Journal of Hydrometeorology*. DOI 10.1175/JHM-D-20-0283.1.

Figure 6: Accumulated equivalent precipitation volume per event at Cabramurra NSW, measured by the PARSIVEL disdrometer. Each event is segregated by type of precipitation and by frontal and post-frontal periods (red and blue shadings, respectively).

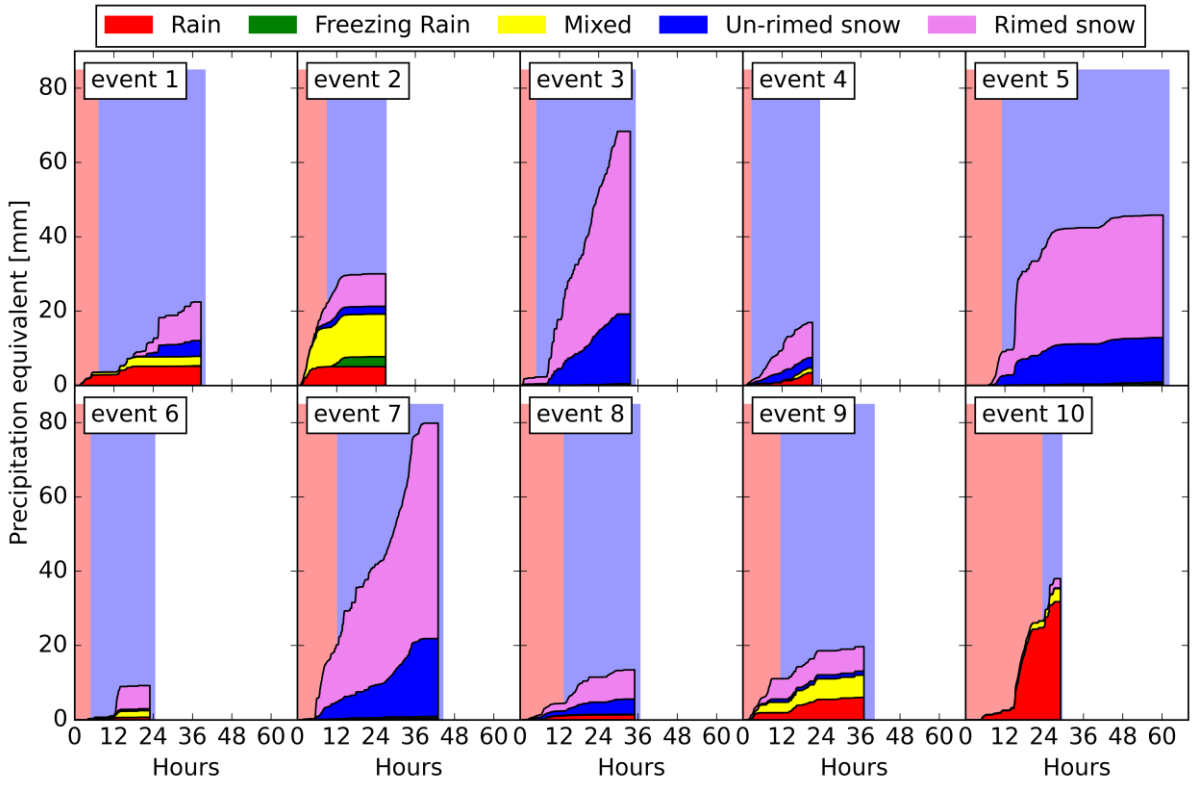

File generated with AMS Word template 1.0

Figure 7: Accumulated equivalent precipitation volume per event at Cabramurra NSW, measured by the PARSIVEL disdrometer. The bar plots show the percentage of precipitation by type for the combined frontal periods (hatched) and post-frontal periods (solid). The right panel shows mean particle concentration per diameter bin with respect to particle diameter for the whole campaign segregated by type with shaded areas showing ± 1 standard deviation.

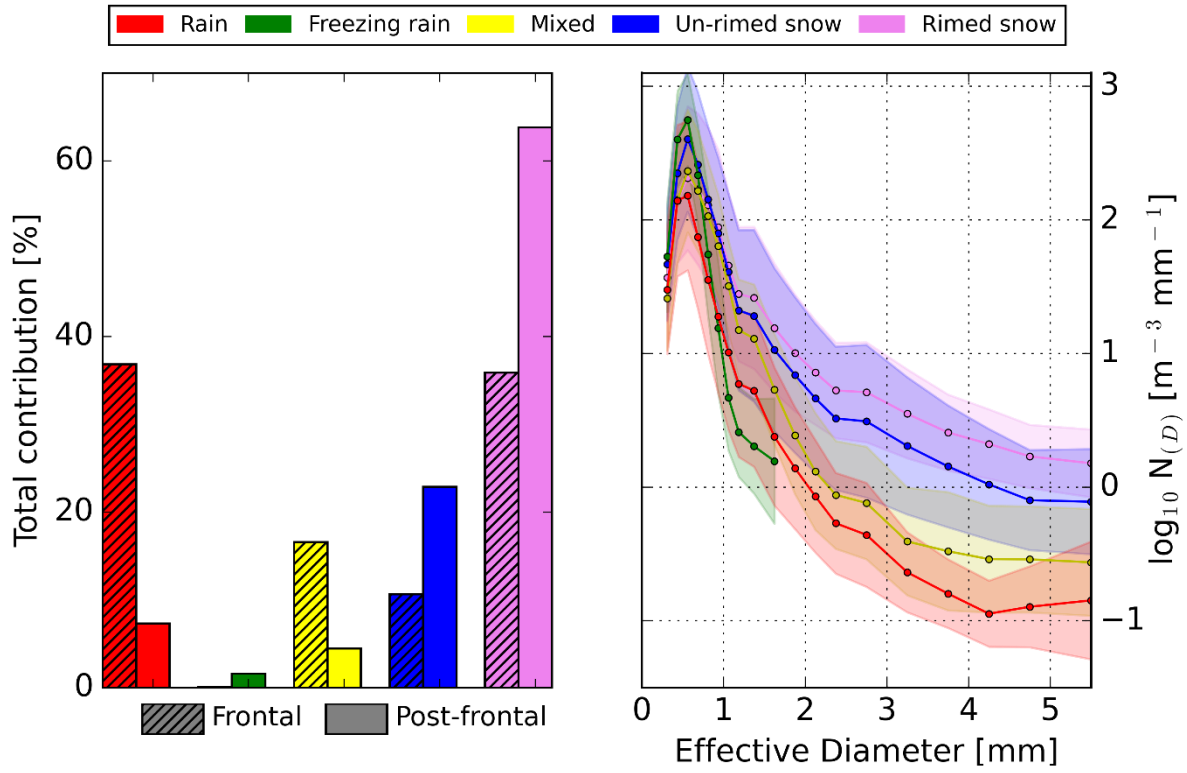

Accepted for publication in *Journal of Hydrometeorology*. DOI 10.1175/JHM-D-20-0283.1.

Figure 8: Left panel shows the MSLP and front locations for the first case study. Right panel shows the MSLP and front locations for the second case study. The red box shows the approximate location of the campaigns area of interest. MSLP diagrams from Australian Bureau of Meteorology.

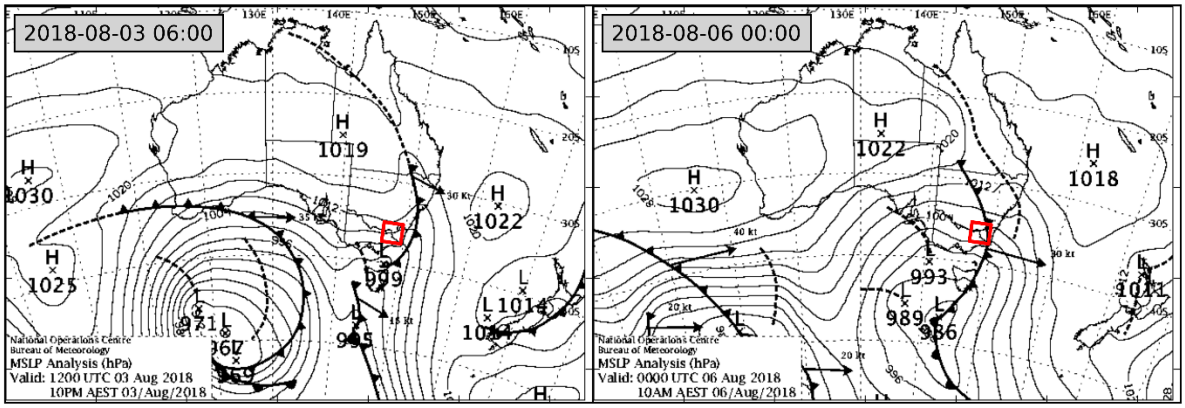

File generated with AMS Word template 1.0

Accepted for publication in *Journal of Hydrometeorology*. DOI 10.1175/JHM-D-20-0283.1.

Figure 9: Radiosondes launched from Khancoban before (A) and after (B) the passage of the cold front during case study 1, grey lines show simulated lifted parcels. Panels C & D show Himawari-8 cloud top temperatures for these periods. Red lines in the bottom panels show 24 hours HYSPLIT back trajectories initiated at 500 m AGL.

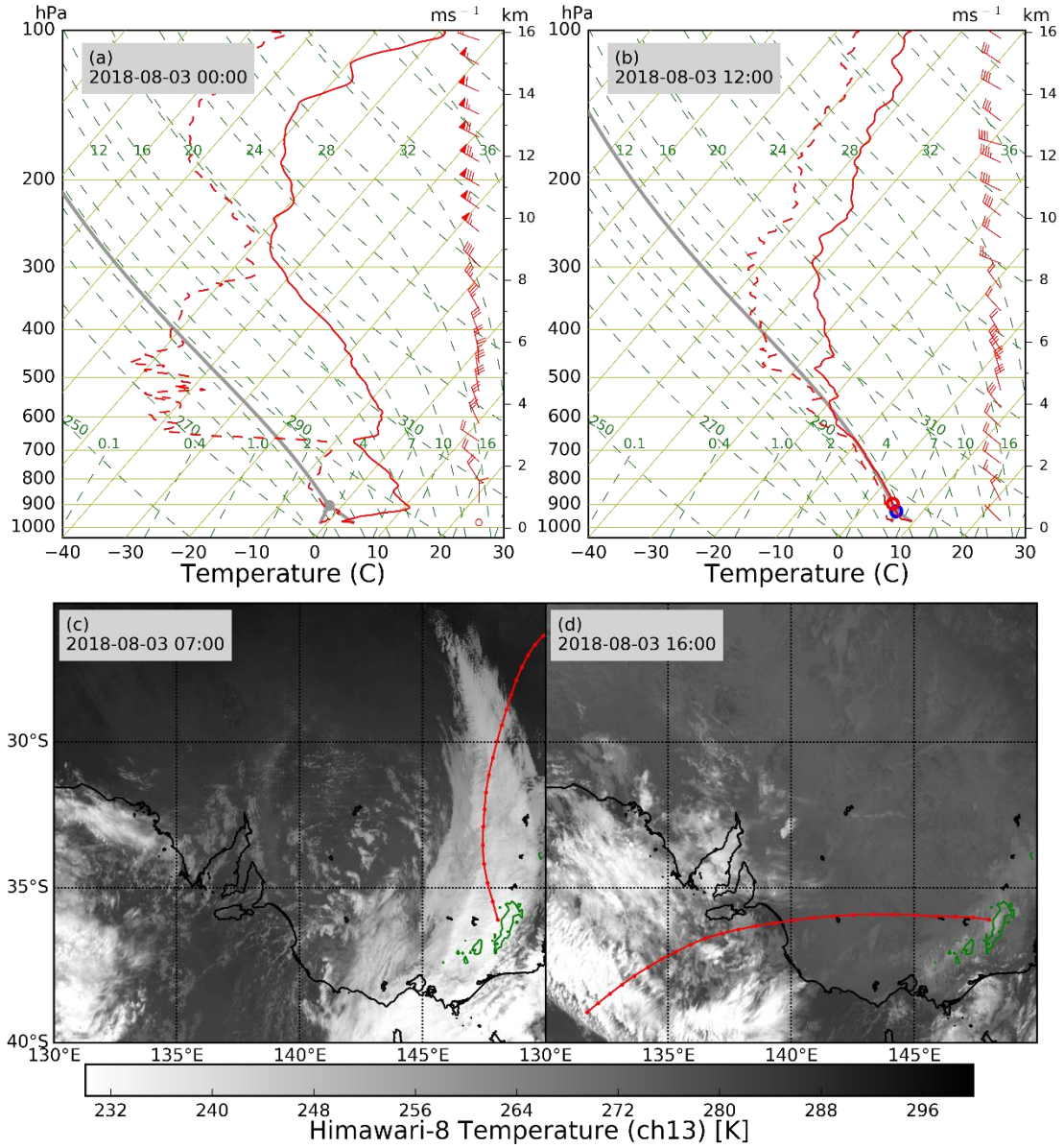

File generated with AMS Word template 1.0

Figure 10: Time series of (from top to bottom) BASTA equivalent radar reflectivity (left y-axis) and cloud-top height (right y-axis), MRR equivalent radar reflectivity (left y-axis) and ambient temperature (right y-axis), MRR radial velocity (left y-axis) and wind speed (right y-axis), and precipitation intensity (left y-axis) and $\hat{H}^2$ (right y-axis) at Cabramurra during the first case study. The frontal and post-frontal time periods selected to create the CFTDs of Figure 10 are shown in dashed boxes in the MRR radar reflectivity panel. The vertical dashed line shows the transition from frontal to post-frontal. Note that the wind barbs are in m s^{-1}.

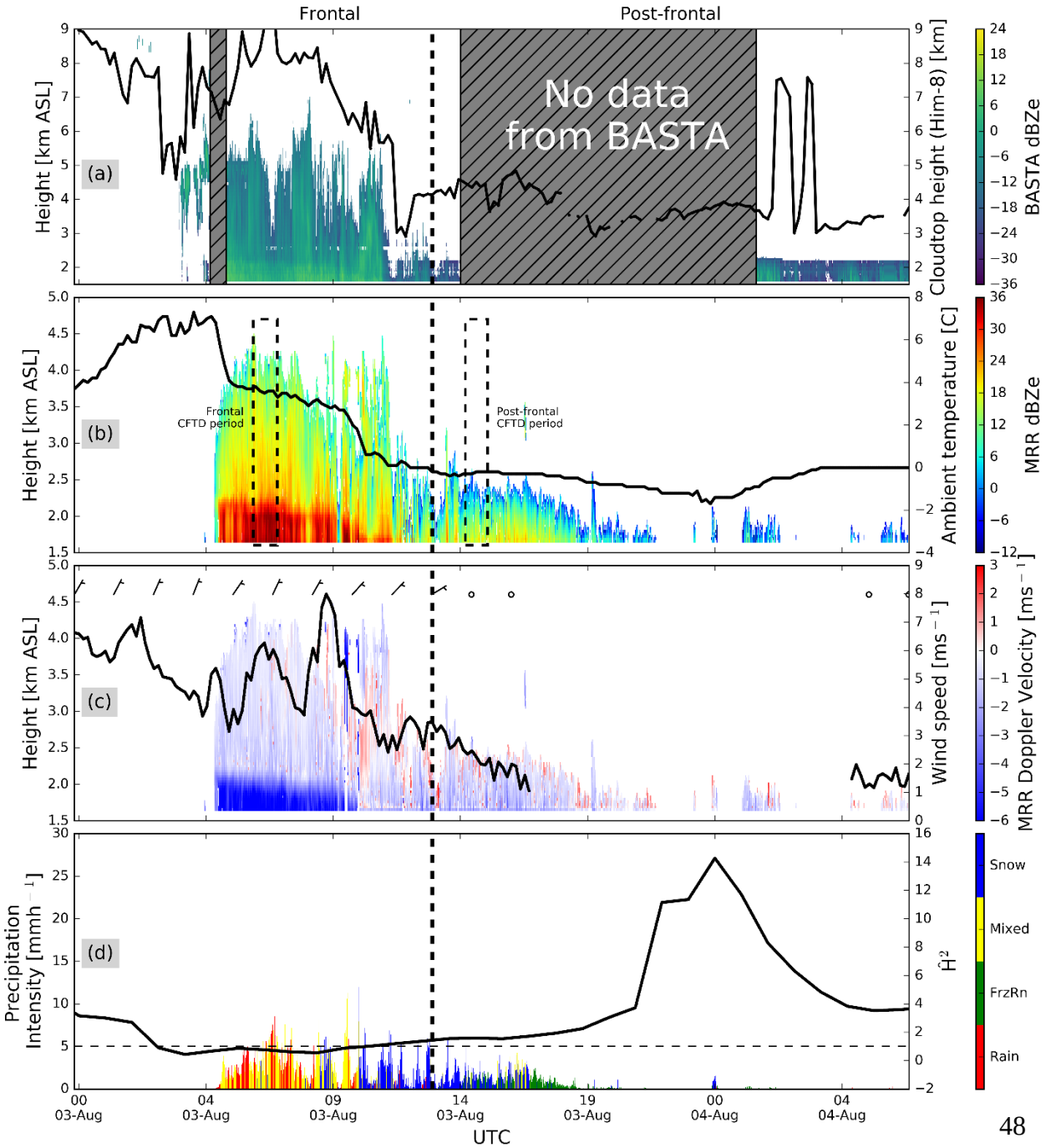

File generated with AMS Word template 1.0

Accepted for publication in *Journal of Hydrometeorology*. DOI 10.1175/JHM-D-20-0283.1.

Figure 11: Case study 1 reflectivity and radial velocity CFTDs from Murray 1 (bottom panels), Cabramurra (middle panels), and Blue Cow (top panels) segregated between frontal (left panels) periods and post-frontal (right panels) periods.

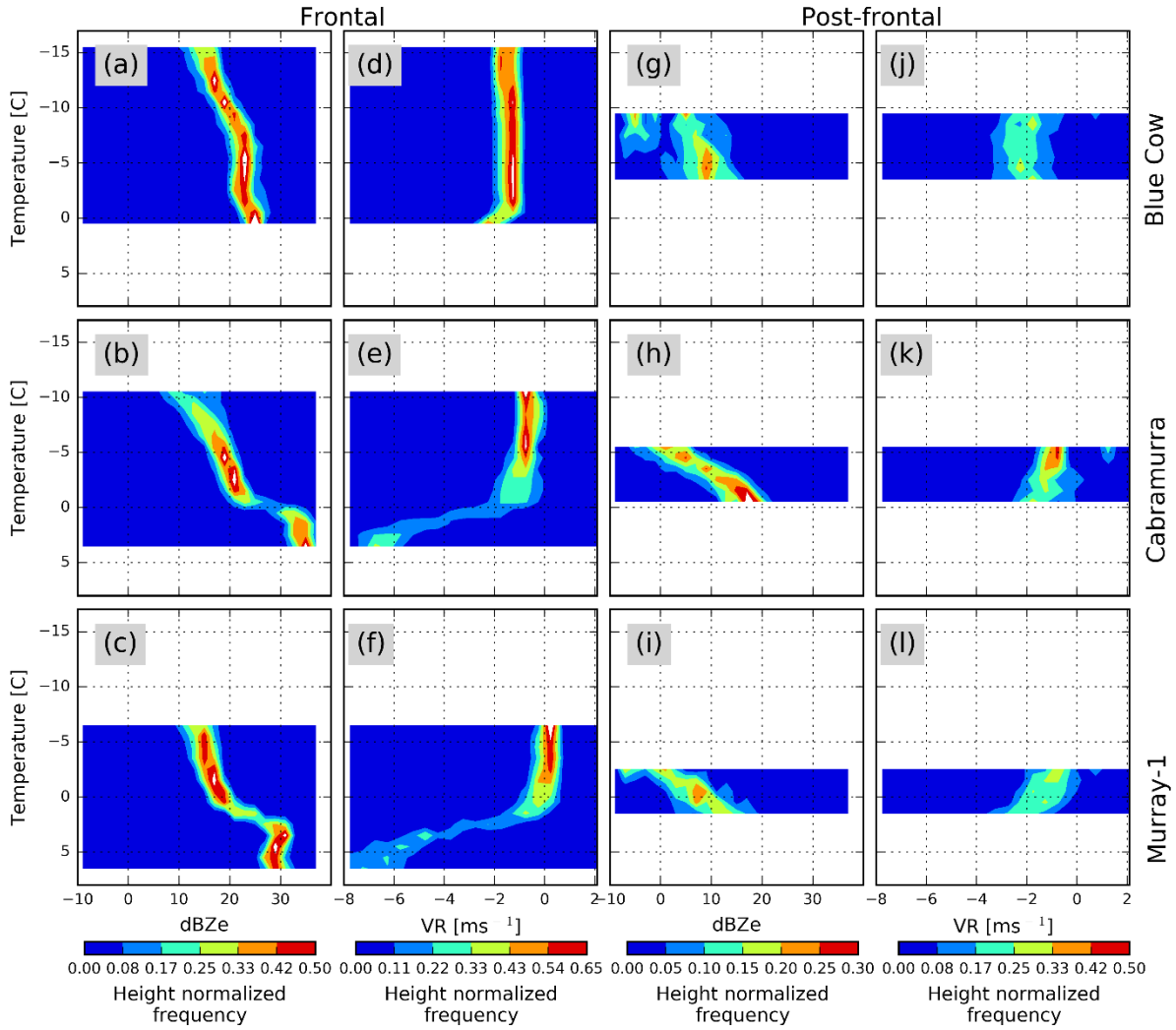

File generated with AMS Word template 1.0

Figure 12: Radiosondes launched from Khancoban (top panels) during the passage of the cold front (left) for case study 2, grey lines show simulated lifted parcels. Top-middle and top-right panels show radiosondes for the convective and stratiform parts of the post-frontal period respectively. Bottom panels show Himawari-8 cloud top temperatures for these periods. Red lines in the bottom panels show 24 hours HYSPLIT back trajectories initiated at 500 m AGL.

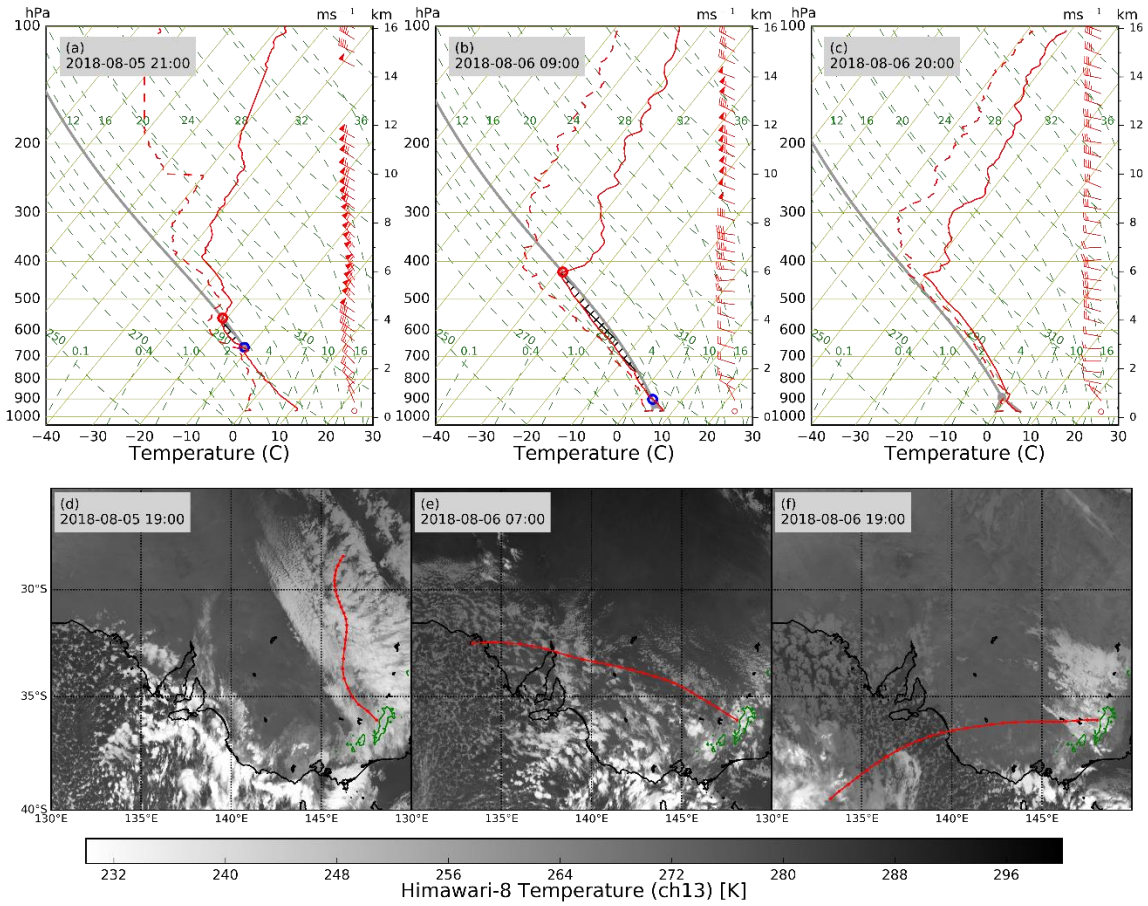

File generated with AMS Word template 1.0

Figure 13: Time series of (from top to bottom) BASTA equivalent radar reflectivity (left y-axis) and cloudtop height (right y-axis), MRR equivalent radar reflectivity (left y-axis) and ambient temperature (right y-axis), MRR radial velocity (left y-axis) and wind speed (right y-axis), and precipitation intensity (left y-axis) and $\hat{H}^2$ (right y-axis) at Cabramurra during the second case study. The convective and stratiform time periods selected to create the CFTDs of Figure 13 are shown in dashed boxes in the MRR radar reflectivity panel. The vertical dashed lines show the transition from frontal to post-frontal convective, and then to post-frontal stratiform. Note that the wind barbs are in m s^{-1}.

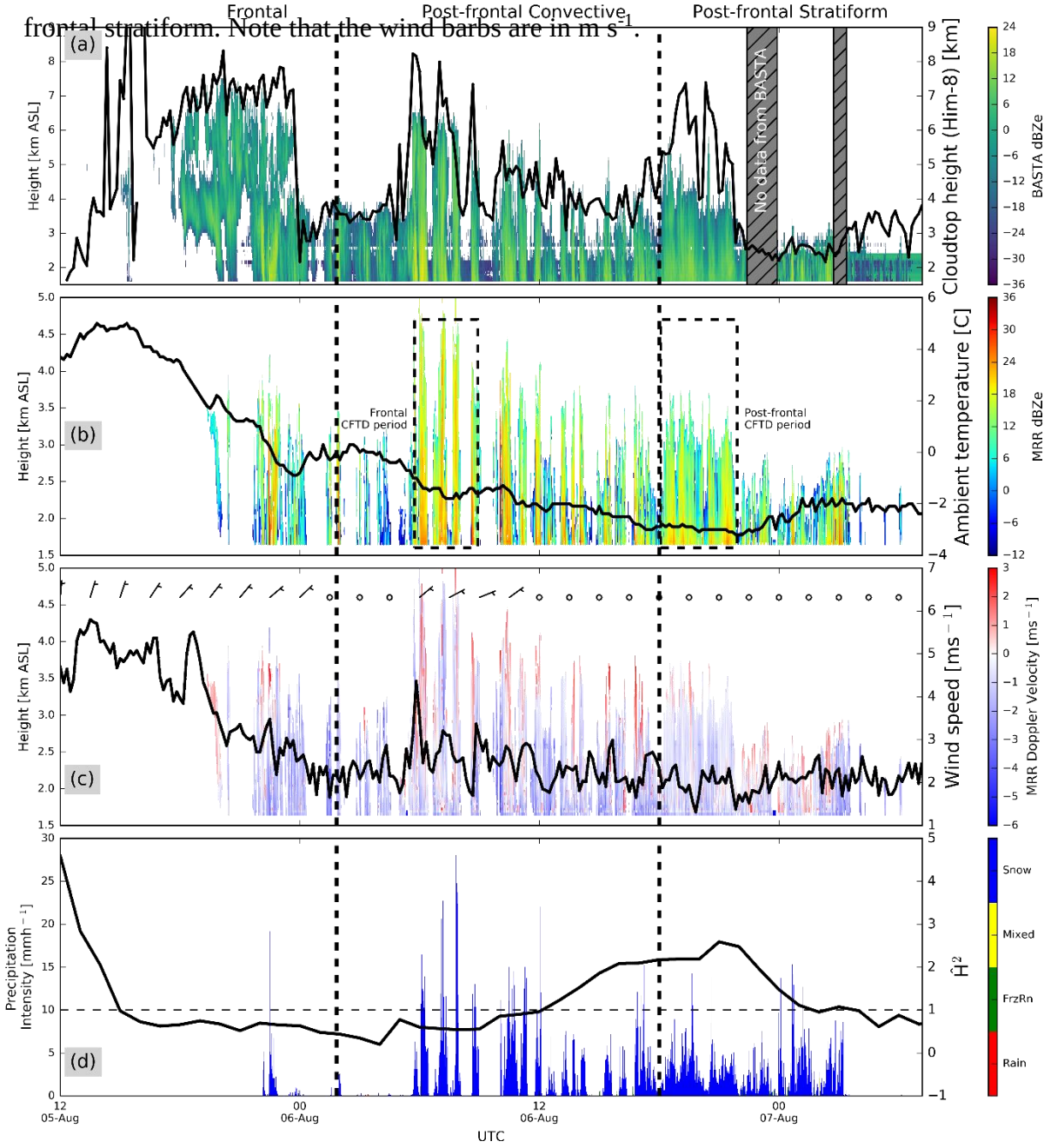

Accepted for publication in *Journal of Hydrometeorology*. DOI 10.1175/JHM-D-20-0283.1.

Figure 14: Case study 2 reflectivity and radial velocity CFTDs from Murray 1 (bottom panels), Cabramurra (middle panels), and Blue Cow (top panels) segregated between convective (left panels) period and stratiform (right panels) periods.

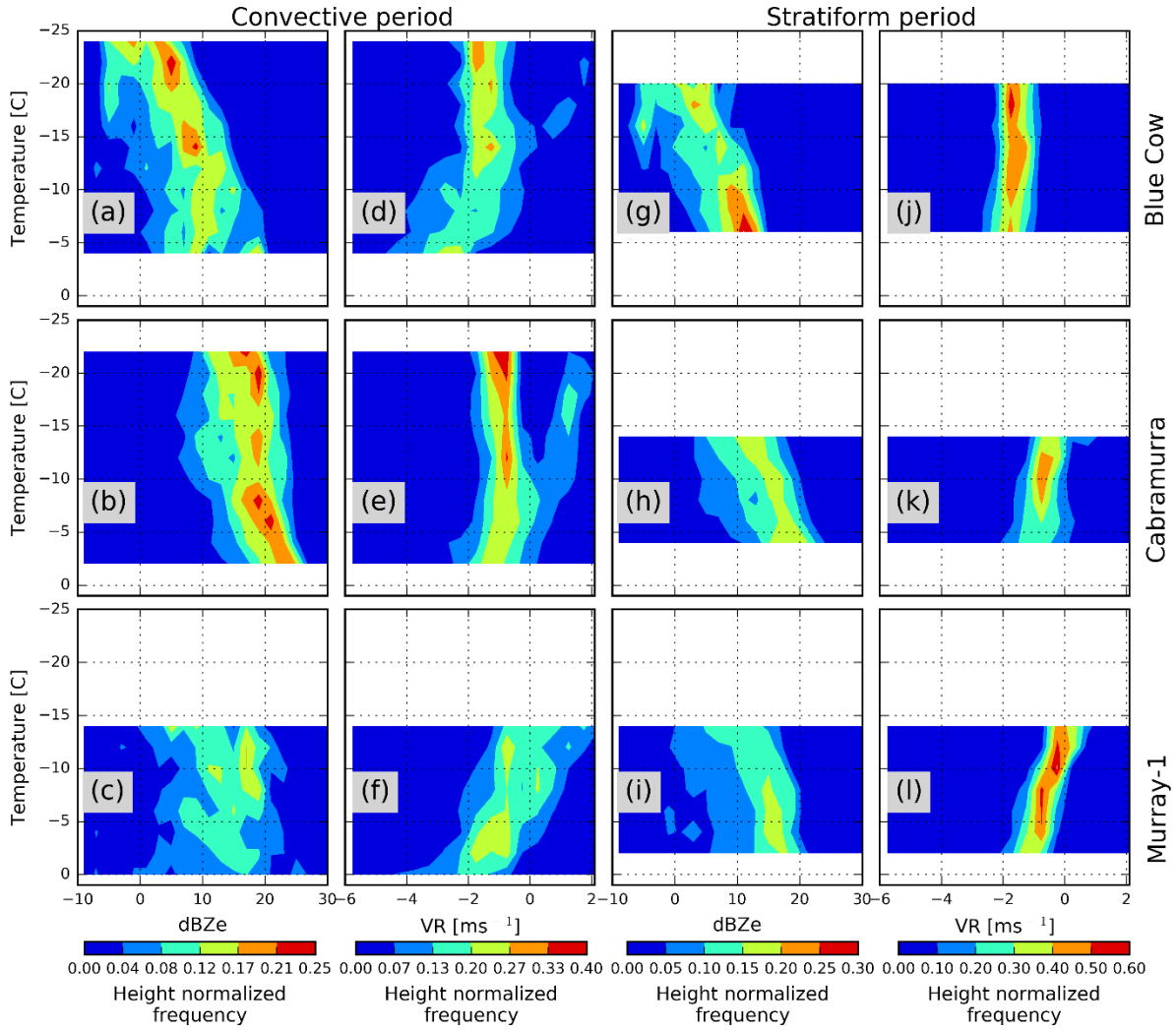

File generated with AMS Word template 1.0